Simultaneous vascular strain and blood vector velocity imaging using high frequency versus conventional frequency plane wave ultrasound: a phantom study

Stein Fekkes*, Anne E. C. M. Saris*, Maartje M. Nillesen, Jan Menssen, Hendrik H. G. Hansen, Chris L. de Korte

***Abstract*— Plaque strain and blood vector velocity imaging of stenosed arteries are expected to aid in diagnosis and prevention of cerebrovascular disease. Ultrafast plane wave imaging enables simultaneous strain and velocity estimation. Multiple ultrasound vendors are introducing high frequency ultrasound probes and systems. This study investigates whether the use of high frequency ultrafast ultrasound is beneficial for assessing blood velocities and strain in arteries. The performance of strain and blood flow velocity estimation was compared between a high frequency transducer (MS250, fc = 21 MHz) and a clinically utilized transducer (L12-5, fc = 9 MHz). Quantitative analysis based on straight tube phantom experiments revealed that the MS250 outperformed the L12-5 in the superficial region: low velocities near the wall were more accurately estimated and wall strains were better resolved. At greater than 2 cm echo depth, the L12-5 performed better, due to the high attenuation of the MS250 probe. Qualitative comparison using a perfused patient-specific carotid bifurcation phantom confirmed these findings. Thus, in conclusion, for strain and blood velocity estimation for depths up to ~2 cm a high frequency probe is recommended.**

***Index Terms*— displacement estimation, flow estimation, high frequency ultrasound, PVA phantom, plane wave ultrasound, strain imaging**

I. Introduction

DEVELOPMENT of atherosclerosis in the carotid artery (CA) may lead to severe stenosis obstructing the main cerebral blood flow supply due to geometrical changes of the luminal area. It also initiates compositional changes due to the development of calcifications, lipid pools, fibrous tissue, and haemorrhages in the vessel wall, which could lead to the formation of rupture prone plaques. These pathological processes can be asymptomatic for a long time until the initiation of a fatal event such as a stroke or transient ischemic attack. This is why characterization of atherosclerosis is important to guide pharmaceutical treatment or perform an invasive intervention removing suspected critical obstructions in the CA.

In clinical practice, ultrasound imaging is mostly used for plaque stenosis grading. The stenosis is usually visualized using duplex ultrasound (B-mode and Colour Flow Imaging (CFI)), followed by Pulsed Wave (PW) Doppler acquisitions to measure the maximum systolic blood velocity in the area of the most severe vessel narrowing and in a post stenotic segment of the lumen. From this information, a coarse estimate of the degree of stenosis can be derived [1]. Although the potential of diagnostic ultrasound to classify and grade carotid disease is recognized, so far there is no universally accepted protocol to measure the degree of stenosis [2].

A main reason for the lack of a universal guideline is the considerable variability in estimated velocities using Doppler techniques [3], which might result in errors of the estimated grade of stenosis. The large variability can be assigned to multiple limitations of conventional Doppler techniques, of which the angle dependency is a major contributor [2]. The angle between the insonifying beam and the (local) blood flow direction is required to convert the 1D velocity estimate, measured along the beam direction, into a velocity estimate in the true direction of the blood flow. This angle is difficult to estimate when looking at non-laminar flow patterns in the carotid artery that are known to be present in the bifurcation and in stenosed regions [4-8]. Another major limitation of conventional Doppler-based methods is the use of conventional line-by-line acquisition schemes, which limits the frame rate and/or imaging view substantially. Furthermore, the span of velocities that can be determined is limited by the pulse repetition frequency due to aliasing.

Major effort has been put into the development of 2D and 3D blood vector velocity imaging techniques that circumvent the

*Both authors contributed equally. Manuscript submitted October 10, 2017. This research is supported by the Dutch Technology Foundation STW (NKG 12122), which is part of the Netherlands Organization for Scientific Research (NWO), and which is partly funded by the Ministry of Economic Affairs. S. Fekkes, A.E.C.M. Saris, M.M. Nillesen, J. Menssen, H.H.G. Hansen and C.L. de Korte are with the Medical UltraSound Imaging Center, Department of Radiology and Nuclear Medicine, Radboud university medical center, Nijmegen, the Netherlands, www.radboudmusic.nl. C.L. de Korte is also with the Physics of Fluid Group, MESA+ Institute for Nanotechnology, and MIRA Institute for Biomedical Technology and Technical Medicine, University of Twente, Enschede, The Netherlands. Corresponding author: Anne E.C.M. Saris, Anne.Saris@radboudumc.nl This paper has supplementary downloadable materials available provided by the authors. This includes a video clip ClutterFiltering.mp4 showing the effect of clutter filtering (15 MB) and StrainAndBloodFlowDynamics.mp4 which shows the strain and blood velocity dynamics (32 MB).

angle dependency. Several methods have been suggested, amongst others, Vector Doppler [9], Transverse Oscillation [10], Speckle Tracking (ST) [11] and directional beamforming [12]. All proposed methods are capable of providing estimates of the 2D velocity vector in the scan plane, thereby providing a more reliable representation of the physical flow field.

As explained, Duplex ultrasound is mainly used to derive parameters related to stenosis geometry. However, it does not provide information about the plaque composition. Characterization of the composition is of paramount importance, because pathology studies have shown that the presence of a large lipid core that is covered by a thin fibrous cap is associated with an increased risk for rupture which might subsequently lead to a cardiovascular event [13, 14]. Differentiation between stable and rupture-prone plaques is one of the major challenges in cardiovascular research [15]. Mechanical characterisation of the plaque, using ultrasound strain imaging or elastography [16, 17], can provide such information. By estimating strain in response to blood pressure pulsations, mechanical properties and plaque composition can be revealed indirectly [18-20]. Both intravascular [15, 21-26] and non-invasive [27-41] vascular strain imaging studies have been conducted and showed that regions with higher strain values correspond to plaques with a large lipid core.

Recent development in ultrasound technology and computational power enable plane wave and diverging wave imaging. Unfocused ultrasound transmission followed by parallel receive beamforming allows imaging at acquisition rates up to 20 kHz, which facilitates imaging the dynamics of both tissue and blood. Ultrafast imaging has already been applied to image blood velocities in the carotid artery [7, 42-45] and to assess the arterial wall dynamics using both pulse wave velocity [46] and elastography [47-49].

Plaque extent and vulnerability, derived from local strain estimates, together with accurate and reproducible measurements of the dynamically complex velocity blood flow patterns are expected to allow for a more complete characterisation of atherosclerosis, thereby aiding the clinician in establishing a fast and reliable judgement about the stage and progression of arterial disease. With ultrafast imaging strain and 2D blood velocities can be obtained simultaneously from the same acquisition [50-52]. However, one drawback of the ultrafast techniques is that the images have a reduced contrast- and signal-to-noise ratio and lower lateral resolution [53], due to the lack of focusing in transmit. Displacement compounding is a technique that can be used to circumvent the use of this low resolution lateral information [54, 55]. Both tissue strain and blood velocities can be estimated accurately using this technique combined with plane wave acquisitions [48, 49, 56]. Another possible way to cope with the adverse resolution effects of ultrafast imaging, is by using high frequency ultrasound (>20 MHz). Since the carotid artery is located at shallow depths, it could be an excellent application for high frequency ultrasound imaging. The increased resolution and the elevated blood signal power, which are inherent to the use of high frequency ultrasound, could be beneficial for strain and blood flow imaging of the carotid artery. However, this is counter balanced by increased attenuation values. Another reason for exploring the potential of high frequency ultrafast ultrasound is the trend in the development of high frequency ultrasound probes. Several manufacturers, like Toshiba Medical (Aplio i-series), Philips, BK Ultrasound and Visualsonics are developing these probes and bringing them to the market for *in vivo* imaging of, mainly, musculoskeletal and superficial vascular structures in humans.

Therefore, this study compares the performance of a high frequency transducer with a clinically utilized transducer for the assessment of tissue strain and blood flow using a sophisticated bifurcation phantom that is based on an *in vivo* geometry obtained in a patient. The accuracy and precision of the strain and velocity measurements is evaluated by experiments using straight cylindrical phantoms. To our knowledge, the combination of plane wave imaging and high frequency ultrasound has not yet been explored to visualize and quantify the dynamics of both the carotid vessel wall and blood velocities.

II. Methods

For consistency, the imaging acquisition sequence, post-processing of radio-frequency (RF) element data, and the displacement estimation, including clutter filtering, as described in this section are kept the same for all conducted experiments.

A. Imaging setup

An L12-5 ATL linear array and an MS250 Visualsonics linear array were used in all experiments. Both transducers were connected to a Verasonics Vantage ultrasound system (Verasonics, Kirkland, WA, USA). The Vantage system was equipped with a UTA 360 transducer adapter (Verasonics, Kirkland, WA, USA) to provide compatibility with the MS250 transducer from Visualsonics. Ultrasound RF element data were acquired for both transducers by transmitting zero-degree plane waves at a pulse repetition frequency (PRF) of 4 kHz for 1 second, i.e., one pressure cycle. The transducer properties and acquisition parameters are listed in Table I.

B. Beamforming grid and RF data reconstruction

Plane wave imaging permits data reconstruction, i.e., the conversion of unfocused RF element data into beamformed RF data, at any location within the insonified region. We recently showed that customization of the beamforming grid according to the system's point-spread-function (PSF) facilitates improved subsample displacement estimation [57]. Since speckle size is proportional to the dimensions of the imaging system's resolution cell [58], i.e., the PSF, a spatial auto covariance method [59] was used to determine the speckle size (full width half maximum) using B-mode images of the phantom. The resulting spacing for both grids is listed in Table II, together with other beamforming parameters. Delay-and-sum beamforming was used to generate RF data for every plane wave emission.

C. Strain and velocity estimation

Inter-frame 2D displacements were estimated using a 2-step, 2D normalized cross-correlation (CC)-based method. In the first iteration, displacements on sample resolution were estimated using demodulated RF data. The second iteration, based on RF data, was initiated using the sample offset acquired in the first iteration, and resolved sub-sample resolution displacements. Subsample resolution was resolved by 2D interpolation of the CC function. The kernels sizes used for both transducers were kept similar in size with respect to the number of RF or envelope data points. The size of the search kernel in iteration 1 was tuned to the maximum displacement expected in each experimental situation. Spatial filtering of the 2D inter-frame displacements was performed using a median filter with windows containing an equal number of displacement estimates for both transducers. An overview of the settings used for the displacement estimation can be found in Table III.

Inter-frame axial and lateral displacements in the carotid wall and surrounding tissue were estimated at 100 Hz. Velocities in the lumen were estimated at 4000 Hz by multiplying the inter-frame displacements with frame rate. Thereafter, velocities were averaged over a temporal ensemble of 40 frames, resulting in an effective velocity frame rate of 100 Hz.

To generate a region of interest (ROI) for both the lumen and the surrounding tissue, manual segmentation was performed on a registered, combined overlay of B-mode images from the MS250 and the L12-5. One reference contour was manually marked in the frame corresponding to the 'end-diastolic' frame in the pressure cycle. Thereafter, the contour was tracked over the cardiac cycle using the estimated vessel wall displacements to generate a lumen and tissue ROI at 100 Hz.

D. Clutter filtering (blood velocity estimation)

Prior to inter-frame velocity estimation in the lumen, clutter filtering was performed to suppress the dominant signal of the surrounding tissue. Filtering was performed using finite impulse response (FIR) filters and a temporal sliding window, which enables longer ensemble sizes without sacrificing frames for filter initialization. Two filters were designed, one for the MS250 data and one for the L12-5. Filter orders were scaled according to the difference in center frequencies to obtain similar filter characteristics. Resulting filter orders (N) were 20 and 46 for the MS250 and L12-5, respectively. Based on the spectral content of the RF data, frequency cut-off points were calculated for both transducers such that (axial) velocity cut-off characteristics were similar. The frequency response of the FIR filters and the corresponding cut-off points are summarized in Table IV. For a dynamic visualization of the clutter filter effect the reader is referred to the additional multimedia file: ClutterFiltering.mp4.

E. Tracking and principal strain estimation (vessel wall)

To accumulate the filtered, inter-frame displacements in the vessel wall over the complete pressure cycle, tracking was performed, with the end-diastolic frame as reference frame. 2D linear interpolation was performed to accumulate all inter-frame displacements. Subsequently, strain was determined by taking the first order spatial derivative of the cumulated displacements by applying least-squares strain estimator in axial, lateral and shear directions [60]. Finally, the principal strains [61] were obtained by the eigenvalue decomposition of the symmetric Lagrangian finite strain tensor to exclude rigid body motions and only regard strains originating from pure finite deformations.

III. Experiments

To compare the performance of both transducers in a realistic setting, a bifurcation phantom was created, based on an *in vivo* geometry obtained in a patient. Results obtained for this phantom will be studied qualitatively. Dedicated straight cylindrical vessel phantoms were used to study the precision and accuracy of strain and velocity estimation methods for both transducers.

A. Bifurcation phantom

A patient-specific vessel wall geometry of the carotid artery (CA) (Fig. 1 (a)) at the bifurcation was obtained by segmentation of a preoperatively acquired 3D CT angiography [62] containing an 82%-degree of stenosis. This geometry was then converted into a mold using CAD (Autodesk Inventor 2015, Student version) (Fig. 1 (b), (c)). Next to the CA, a cylindrical, straight tube validation vessel (length = 100 mm, Øinner = 4.75 mm, Øouter = 7.75 mm) was designed. Both vessels were placed in a surrounding mold at a mean averaged depth of 20 mm from the imaging surfaces (Fig. 1 (d)). Subsequently, a synthetic polymer [63] PolyVinyl Alcohol (PVA) Cryogel (Mw 85.0 – 124.0 99+% hydrolyzed, Sigma-Aldrich, Zwijndrecht, The Netherlands) was used to build the phantom. To create the solution, a mixture of 60% by weight (wt %) distilled water, 40 wt % anti-freezing agent (ethylene glycol, Sigma-Aldrich, Zwijndrecht, The Netherlands), 10 wt % PVA and 2.0 wt % Silica gel particles (Merck Kieselgel 60, 0.063 – 0.100 mm, Boom B.V., Meppel, The Netherlands) was heated to ~85° in a closed cylinder until a homogeneous liquid was formed. After injection of the solution into the vessel molds (Fig. 1 (b), (c)) at 50°C, it was degassed for 1 hour before it was subjected to 3 cycles of freezing (-25°C) and thawing (21°C), for 16 and 8 hours, respectively. For the surrounding mold (Fig. 1 (d)), 700 ml PVA (10 wt %) was prepared with 0.5 wt % scatterers to enhance contrast between the vessel walls and the surrounding tissue. After filling the surrounding mold containing the CA and validation vessel, the complete phantom was subjected to an additional last freeze-thaw cycle. Finally, for validation purposes, the Young's modulus was determined (see the Appendix).

B. Validation setup

1) Strain

For strain validation measurements, the validation vessel was pressurized using a pulsatile flow waveform, at 60 bpm, with a mean flow of 0.62 L min-1 and a peak flow of 1.39 L min-1 [64]. A single adjustable flow resistor was set such that the dynamic pressure at systolic phase ranged from 109 mmHg to 141 mmHg, which was sampled with 13 pressure steps

(TruWave pressure transducer, Edwards Lifesciences Corp. Irvine, CA). Image acquisition, displacement and axial strain estimation were performed as described in the Methods section. For analysis, 100 image lines at the center of the probe were used, resulting in a field of view of 3.9 mm and 4.9 mm for the MS250 and the L12-5, respectively. The displacement data were first corrected for global motion of the vessel center. A single reference displacement definition was determined by fitting the displacement data of both probes and segments to a 1/R relation (Fig. 3 red lines). Based on linear elastic behavior of the phantom, the displacement estimates were normalized using the pressure at the maximum pressure level. A least-squares fit was performed to obtain the reference displacement at maximum pressure. This reference was de-normalized using the pressure to obtain a reference displacement belonging to each pressure state. Please note that this method enables a single reference fit based on multiple deformation states which result in a more robust and trustworthy reference displacement. The reference strain was calculated using the spatial derivative of the reference displacement. For performance evaluation, four spatial segments were defined which were: the superficial surrounding, superficial vessel wall, deeper vessel wall, and deeper surrounding. The performance was expressed by the mean relative bias and the mean relative standard deviation (SD) of the 100 lines for each spatial segment. Relative measures were obtained by dividing bias and SD by the reference strain.

2) Flow

For flow validation, measurements were conducted in a straight tube flow setup, with Blood Mimicking Fluid (BMF-US, Shelley Medical Imaging Technologies, Canada) circulating through the system at a constant flow rate of 1.2 L/min by a gear pump (volume flow accuracy of 0.6%, model H3F, Liquifl, Garwood, USA). A 1.5 m long glass entrance tube fixated at a rigid frame ensured fully developed laminar flow with circular symmetric parabolic velocity profiles. The glass tube was extended by a tube of heat-shrinking material inside a tank filled with water, where a perfectly matched glass to heat-shrinking tube coupling was made for smooth fluid transition. The heat-shrinking material was tested to be sufficiently transparent to ultrasound. The bottom plate of the tank was placed at an angle to avoid reverberations. Via a settling reservoir, the BMF was returned to the pump. The vessel radius of both the glass and rubber tube was 5 mm and the wall thickness of the rubber tube was 300 µm. Both transducers were placed above the tank, fixated in a probe holder, at flow angles of 90° (pure lateral flow) and 75°. The tube was placed at a depth corresponding to the elevational focus of both transducers, see Table I. The theoretical velocity profile was calculated based on the applied flow rate and vessel geometry, resulting in an expected peak velocity of 0.51 m/s.

To describe the performance of the velocity estimator, mean bias and SD were calculated for the velocity magnitude and angle, based on 100 estimated ensemble-averaged velocity fields. The magnitude measures were divided by the ground truth velocity magnitude to obtain a relative value. Velocity profiles were studied at the center of the transducer and at 5.5 mm at either side of the center position, meaning statistics were calculated over 300 estimated profiles.

3) Bifurcation phantom setup

The bifurcation phantom was mounted in a bracket supporting the connections to the inlet flow tube at the common carotid artery side and two tubes at the outlet side at the internal and external carotid artery, see Fig. 2. BMF was circulated in a closed loop circuit by a gear pump driven by software written in LabView (National Instruments, Austin TX, USA). A pulsatile flow was applied, similar to the one described in the strain validation paragraph. At both outlet tubes, adjustable flow resistors were set such that the dynamic pressure, measured at the inlet of the CA was 150 over 95 mmHg, mimicking physiologically relevant behavior for a stenosed carotid artery. The flow through the internal carotid artery was measured by a flow meter (probe C-series, flowmeter T107 Transonic Systems Inc, Ithaca NY, USA), which was positioned directly after the outlet side. Setting the flow resistors also allowed for equal division of flow over the internal and external carotid artery. Both transducers, fixated in the probe holder, were attached to a translation stage (see Fig. 2 (b), (c)). This stage facilitated movement of the holder in the lateral direction while maintaining the in-plane orientation, which was used to center the transducers at the same lateral position with respect to the phantom (see Fig. 2 (b), (c)). The transducers were positioned in such a way that the bifurcation was imaged in the longitudinal plane, with the imaging plane orthogonal to the vessel. Subsequently, flow data measured by the flow meter were acquired simultaneously with the ultrasound data using a common trigger generated by the Labview program at the start of the flow waveform. The acquired ultrasound data were processed as described in the Methods section and estimated strain and velocities were evaluated and compared qualitatively for both transducers.

IV. Results

A. Validation setups

1) Strain

The validation vessel was used to assess the performance of displacement and strain estimation in the vessel wall and surrounding tissue for both probes. Fig. 3 depicts the estimated and reference displacement for the MS250 and the L12-5 divided into four segments. The reference fit normalized on the maximum pressure state showed a root mean squared error of 11.8 µm and an r^2 of 0.92. The B-mode representation and its overlay with the reference and estimated displacements indicates overall good agreement for all segments and for both probes except at depths greater than ~25 mm for the MS250. For visualization purposes only 5 out of 13 displacement curves (yellow) are shown within a black area indicating plus or minus 1 SD. The red line represents the reference displacement. The calculated mean bias and mean SD for each spatial segment (A-H) are listed in Table V.

The displacement graphs in Fig. 3 indicate that the superficial surrounding (A, E) shows overall good agreement for both probes. Differences can be observed at the superficial vessel wall (B, F) where the L12-5 shows a bias of -9.6% versus a bias

of -3.5% for the MS250, indicating a stronger displacement underestimation for the L12-5. The same observation holds for the deep wall (C, G) where a mean bias of -11.3% was found for the L12-5 versus a mean bias of -7.5% for the MS250. Please note that both probes are underestimating the displacement near the vessel wall – blood transition likely due to the presence of clutter in combination with the window-based displacement estimation algorithm and filtering procedures. The B-mode images reveal that the ultrasound energy (as represented by the speckle brightness) was focused in the superficial segment (A, B) for the MS250 and in the deeper part (G, H) for the L12-5. As a result, the deep surrounding (D) of the MS250 shows an extraordinary large mean bias of 65%. The L12-5 clearly outperforms the MS250 in that region, with a mean bias of -5.8%. The preference for the L12-5 at the deeper segments (D, H) is also expressed by the difference in mean SD of the MS250 versus the L12-5 of -24.7% and -7.4%, respectively.

Fig. 4 depicts the estimated and reference strain profiles for all segments derived from the estimated and reference displacements in Fig. 3. Due to the asymptotic nature of the strain reference, large deviations were observed at the vessel wall resulting in a large mean bias for the superficial and deeper vessel wall (B, C, F, G), as listed in Table V. The MS250 outperforms the L12-5 regarding the maximum superficial and deep strain estimate of -5% and -4.4% versus the L12-5 maximum strain estimate of -3.3% and 3.2%, respectively. Please note that for the deeper segments (C, H), the location of the maximum for the MS250 is closer to the lumen in comparison to the L12-5.

2) Flow

The straight tube flow setup is used to evaluate the performance of the velocity estimation method for both transducers. The mean and SD of the 300 estimated velocity profiles are shown in Fig. 5 for the velocity magnitude and angle separately. Dotted lines indicate the theoretical profiles, solid lines represent the mean of the estimated profiles and the gray area corresponds to plus or minus one SD. Panel A presents the results for a beam-to-flow angle of 90°, panel B for 75°. The resulting statistics are summarized in Table VI. The estimated profiles closely follow the theoretical profiles, apart from the incorrect estimates close to the deep wall. The large deviations, most dominantly present at a 90° beam-to-flow angle, are due to a high impedance mismatch between the tube and the surrounding fluids (water and BMF), causing strong reflections and reverberations, as also described earlier by others [65, 66]. This, combined with the effects of the clutter filter, distorts the velocity estimates locally. Since this artifact originates from the design of the experimental setup and will not be present for the bifurcation phantom or *in vivo* measurements, statistics were calculated using only the central 90% of the lumen area. Note that the theoretical beam-to-flow angles are not exactly located at 90 and 75 degrees. Because it is difficult to perfectly set the beam-to-flow angle in the measurement setup, the effective beam-to-flow angles were estimated based on the B-mode images obtained from the plane wave data.

The velocities were estimated accurately with a bias of less than 5% for both transducers and flow angles. The positive bias indicates a small overestimation of velocity magnitude. The relative mean velocity bias as well as the SD for the MS250 were slightly lower as compared to the L12-5. The flow angles were also accurately found using both transducers with a mean bias of maximal -0.25°. There is a small reduction in angle SD when using the MS250 with respect to the L12-5 transducer. Differences in magnitude and angle bias between the transducers were mainly caused by the effects near the vessel walls. The high frequency transducer was able to estimate the velocities in those regions more accurately.

B. Bifurcation setup

In Fig. 6, panel (a) B-mode images are presented before and after clutter filtering, which allows for visual comparison between the data obtained using both transducers. The higher resolution for the MS250 probe, as represented by the finer speckle appearance, can be appreciated, as well as the sharper vessel wall to lumen boundary delineation. Furthermore, the increased attenuation for the high frequency probe is clearly visible. Especially in the clutter filtered data, almost no blood signal is visible for deeper parts of the lumen area. Next to that, a shadowing and mirroring artifact is visible underneath the flow divider for both transducers, caused by the refraction of ultrasound, which originates from the specular reflection at the smooth interface between lumen and vessel wall. A quantitative comparison between the signals at two position was performed, as indicated by lines a and b in the B-mode images. Mean signal intensities were calculated and visualized in panel (b). Blood signal intensities (I_B) were calculated by taking the mean over the cardiac cycle of the envelope data after clutter filtering, while the clutter and blood intensities (I_{CB}) were found by averaging before clutter filtering. Then, the clutter signal intensities (I_C) were found by subtracting the blood signal intensities (I_B) from the total clutter and blood signal intensity (I_{CB}). The MS250 data provides the best clutter-to-blood intensity (I_C-I_B) in the lumen of the external carotid artery (position a, upper) of ~12 dB, whereas the L12-5 only has a ~21 dB clutter-to-blood intensity. The average blood intensity in this region is larger for the MS250 data, -47 dB compared to -52 dB for the L12-5, mainly caused by the fact that blood scattering is proportional to the center frequency of the transducer. At larger depths, in the internal carotid artery (position a, lower) and the common carotid (position b), the average blood intensities of the MS250 drop below the intensities for the L12-5, due to stronger attenuation. Since the clutter signals are also attenuated, the clutter-to-blood intensities remain high for the MS250. The larger amount of attenuation for the MS250 can also be appreciated from the average clutter intensities deeper into the phantom. Mean clutter intensities for the L12-5 are ~ -10 till -30 dB, while the mean clutter intensity for the MS250 is at least twice as low, ~ -25 till -55 dB.

Fig. 7 depicts the B-mode image of the bifurcation. The B-mode signal of the vessel wall and surrounding tissue are overlaid with a color-coded strain value and direction vectors.

This article has been accepted for publication in a future issue of this journal, but has not been fully edited. Content may change prior to final publication. Citation information: DOI 10.1109/TUFFC.2018.2834724, IEEE Transactions on Ultrasonics, Ferroelectrics, and Frequency Control

The strain visualized is a combination of the eigen-decomposition which results a minimal negative (compressive) and a maximum positive (tensile) strain component. The classification is made based on the maximum absolute eigenvalue, i.e. the direction in which the maximum deformation occurs.The maximum strain image was calculated at the peak pressure of the systolic phase. Since the resolution of the images is scaled with the center frequency while the filter and window settings are kept equal in sample points, differences in strain distribution smoothness (spatially) are observed and expected. It also accounts for the reduced maximum strain values observed in the L12-5 compared to the MS250.

Strains are predominantly directed normal to the lumen-vessel wall boundary. Considering the upper vessel wall, the MS250 shows a spatial offset of the maximum strain region with respect to the lumen-vessel wall boundary. Maximum strain was expected exactly at the border, especially considering the higher spatial definition of this transducer, as described in the previous paragraph. Probable causes of this induced artifact are the combination of hard reflective acoustic behavior of the blood - PVA vessel wall transitions perpendicular to the ultrasound plane wave and the manual segmented blood-vessel wall inaccuracies.

The flow divider shows a dominant lateral compressive strain component due to the reaction force delivered to separate the blood stream into the internal and external vessel. This lateral compressive strain develops towards an axial compressive strain pattern alongside the vessels. Both internal and external vessels dilate simultaneously pushing the middle part, which results in high centralized strains.

Strain distribution values differ between both transducers, while the direction of deformation shows resemblance. The lower part exhibits the most artifact-like areas, where the MS250 does not seem to provide a reliable principal strain estimate throughout the full aperture width, mainly due to the higher amount of attenuation. The L12-5 however, does show feasible strain estimation except at the center of the aperture. The latter seems to be related to the shadowing artifact as described earlier (see also Fig. 6), since the vessel wall separation tissue is axially aligned with the region of strain irregularities.

Fig. 8 shows the obtained blood vector velocity fields and vessel wall strain in the diseased carotid bifurcation model. Three key time points throughout the cardiac cycle are visualized, showing distinct flow patterns and strain features. In panel A, the peak systolic phase is visualized, where highest blood velocities of the cardiac cycle occur. Predominantly forward flow is observed, with peak velocities towards and near the flow divider and in the stenosed internal carotid artery. Furthermore, the onset of a vortex is visible close to the upper wall of the external carotid. The observed vortex flow pattern is smoother for the L12-5 than for the MS250. Distortions in the velocity field of the MS250 are visible at larger depth. For the L12-5, a smooth velocity field is observed, except for the non-axis-symmetric flow pattern visible at the entrance of the internal carotid, which is shown as a local dip, or two distinct peaks, in the flow trajectory. This is probably due to the shadowing and mirroring artifacts as described earlier (see also Fig. 6). These artifacts are even more predominant for the MS250, which results in distorted velocity fields with incorrect velocity directions. Velocities estimated close to the upper wall of the external carotid differ for both transducers. The MS250 shows low velocities close to the wall, whereas the estimated velocities by the L12-5 are (close to) zero. A frame in the systolic deceleration phase is shown in panel B. Full vortex formation is visible at the entrance of the external carotid, which will remain present also in diastolic phase. Both transducers are capable of capturing this complex low velocity, swirling flow pattern. Panel C shows a frame in late diastole, where low velocities dominate. All three panels show the presence of secondary flows in the external carotid artery. It looks like blood is coming from the vessel wall, however, it is actually coming from the surrounding planes and it is moving into the imaging plane, which is caused by the geometry of the lumen [67]. This effect is less visible in the L12-5 results as compared to the MS250 results.

Regarding the principal strain distribution in panel A, at maximum blood velocity in the peak systolic phase, an overall strain gradient propagating into the surrounding tissue of both transducers can be appreciated. The strain starts to develop and exposes a vessel wall like delineation for the upper and middle part for the MS250. The MS250 lower region starts to show unrealistic strain estimations in contrast to the L12-5. Panel (b) and Fig. 7 show the maximum strain distribution at maximum distention with respect to the end diastolic frame. The location of the strain artifacts for both transducers, in the lower part of the phantom, coincides with the flow artifact below the flow divider, confirming the cause of these errors. At the end of the cardiac cycle, see panel C, a relatively low residual strain can be appreciated in spite of propagated artifacts throughout the cardiac cycle which resulted in erroneous, high negative strain values.

V. Discussion

In this paper, the potential of ultrafast, high frequency ultrasound imaging for the assessment of vessel wall and blood flow dynamics in the carotid artery was investigated. The performance of a high frequency transducer was compared with a clinically utilized transducer in providing this information.

Firstly, straight tube experiments were conducted to perform a quantitative comparison between both transducers by assessing accuracy and precision for both blood velocity and vessel wall strain estimation. These experiments revealed the ability for estimating the blood velocity magnitude and angle using data obtained by both transducers: low magnitude (< 5%) and angle (< -0.25°) bias and SD values were found for the MS250 and L12-5. The MS250 slightly outperformed the L12-5 close to the vessel wall. Regarding the strain validation, the L12-5 shows an overall good performance which is less depth dependent than the MS250, while the MS250 was able to better resolve high displacements and strain in the vessel wall. The differences are predominantly expressed in a more overall smoothing of the L12-5 estimates instead of a difference in

This article has been accepted for publication in a future issue of this journal, but has not been fully edited. Content may change prior to final publication. Citation information: DOI 10.1109/TUFFC.2018.2834724, IEEE Transactions on Ultrasonics, Ferroelectrics, and Frequency Control

spatial ability to resolve the underlying displacement and strain distributions. However, spatial smoothing will suppress local maxima and minima, explaining the differences in the maximum compressive strain peak near the lumen. Furthermore, the validation reference was based on a theoretical fit using experimental displacement data of both probes together. This might lead to a skewed reference compared to the true displacement field. In order to minimize this skewing and to resolve a reliable reference displacement, a single fit was performed incorporating multiple pressure steps assuming linear deformation of the validation vessel.

Secondly, a sophisticated bifurcation phantom was constructed, based on a patient-specific geometry, to obtain realistic ultrasound data in an experimental setting. Material characteristics and geometry of the phantom were shown to be very similar to the finite element model (see Fig. 1 (a) and the appendix). Despite the lack of heterogeneous tissue composition, like calcifications and lipid-rich regions, realistic flow and pressure could be realized providing realistic strain and velocity fields closely resembling the *in vivo* situation. With respect to the attenuation, the phantom material has values which can be expected in patients and also the depth of the bifurcation corresponds to that in an average patient. However, when a thick subcutaneous fat layer is present, the part of the carotid artery for which strains and flow can be estimated using the high frequency probe might differ. We expect that for regular patients with superficially located arteries it will be possible to also obtain accurate strain and flow estimates in the bottom common carotid arterial wall region.

Blood velocity and vessel wall principal strain results obtained in the bifurcation phantom were compared qualitatively, since no ground-truth values were available. Overall, similar events in the evolution of the principal strain and velocity patterns over the cardiac cycle were visible for both transducers. The most important observed differences between the performances of both transducers can be summarized as follows. First of all, the MS250 was able to provide more local velocity and strain information, caused by the higher axial and lateral resolution within the imaging plane, and by the smaller beamwidth in the elevational direction, causing less averaging within the beam. Similar effects were observed in the flow validation results, showing more accurate velocity estimates close to the vessel wall using the MS250 transducer. At larger depths (> 2 cm), presumably incorrect principal strain and velocities were found by the MS250, due to the higher amount of attenuation, while the L12-5 transducer was still able to estimate credible strain and velocity estimates. Finally, the high frequency MS250 transducer showed the capability of estimating low velocity blood flow close to the vessel wall, at shallow depths. This is most likely caused by the relatively higher blood signal intensity, and thereby a higher clutter-to-blood intensity, which is a direct consequence of using high frequency ultrasound, since the power of blood signal scales with the center frequency to the power of four [68]. Estimating velocities close to the vessel wall is crucial for shear stress analysis, which is reported to be highly involved in the development and destabilization of atherosclerotic plaques [69-72]. The angle dependent displacement estimation sensitivity is related to the spatial resolution defined by the point spread function which, amongst elevational beam width and SNR, is one of the reasons that the MS250 is capable of resolving low blood velocities closer to the vessel wall compared to the L12-5 (see Fig. 8). However, the fact that the L12-5 shows a smoother representation of the vortices for all phases compared to the MS250 is due to a more pronounced spatial smoothing since the smoothing kernels were kept equal in sample points instead of metric units for comparison reasons described earlier. Altogether, the results show the potential of using high frequency ultrasound for imaging vessels at shallow depths, up to 2 cm. This implies that the high frequency probe could be useful in clinic for strain and blood velocity imaging. The high frequency transducer might also be applied to smaller, more superficial arteries, such as the radial artery, although the clinical value of functional imaging of these arteries is yet to be determined.

Due to patient and probe movement, misalignment of imaging planes, physiological variance in blood pressure and resulting blood flow, using *in vivo* data for both quantitative and qualitative performance comparison of two transducers is not feasible. In the presented experimental setting, these variables were well controlled which enabled a qualitative comparison. As described, physiological flow and strain values were obtained in the experimental setting, implying the *in vivo* situation was closely mimicked. However, translating this technique towards in vivo applications will come with some additional challenges. Tissue inhomogeneity's, like calcifications, and larger imaging depths are common for diseased carotid artery scanning and will result in increased attenuation, thereby decreasing the imaging SNR. This will compromise the cross-correlation-based blood flow velocity and strain estimation techniques. The effect of these challenges will be more profound for high frequency imaging than for conventional frequency imaging.

For the validation vessel, the maximum strain should always occur at the vessel wall-blood transition and cannot be dislocated into the tissue. This even holds for differences in Young's moduli of the vessel wall and surrounding as long as circle symmetry applies. The strain distribution at the upper vessel wall-blood transition of the bifurcation phantom shows a dislocation of the highest strain region similar as observed for the straight tube validation. However, since the bifurcation phantom is a 3D complex geometry experiencing complex 3D deformation, one cannot assume circle symmetry and complex strain patterns could arise. As an example; the middle part of the bifurcation (Fig. 8 (b), flow divider), in between the internal and external carotid artery, is compressed from both sides resulting in a high strain region surrounded by lower strain regions. Consequently, strain estimation at vessel wall blood transitions should be considered with care.

Clutter filtering remains one of the major challenges in blood velocity imaging [73-75]. However, the availability of continuous plane wave data allows for filtering using large ensemble sizes, where filter order is no longer limited. In present work, this new flexibility was used for scaling the FIR

filter order according to the center frequency difference of the transducers. The choice for similar filter characteristics, to ensure equal attenuating power, has a direct effect on the data quality after filtering, showing more remaining clutter after filtering for the L12-5 transducer (Fig. 6), due to frequency dependent attenuation and blood pool scattering. Filter characteristics can be further improved by using even higher filter orders, with narrower stopbands and shorter transition regions, making it possible to measure low blood velocities. Furthermore, the use of filters which adapt to surrounding tissue motion, i.e., time varying filters, have the potential to further improve the velocity estimation.

Although speckle tracking can measure velocities beyond the Nyquist limit, velocities higher than the Nyquist velocity will wrap around the velocity scale during the clutter filtering process. This means that several velocities (frequencies) can be attenuated when falling into the stop band or transition region of the clutter filter. Although this effect can be present, especially for the high frequency transducer, the velocity estimation was not, or minimally affected by this. This could be assigned to the fact that speckle tracking is based on the spatial correlation of all available frequencies, i.e., it uses a broad band approach, and therefore, is not directly influenced by the attenuation of several frequencies [76]. This is in accordance with other studies that showed that speckle tracking is able to yield consistent velocity estimates within the filter transition region and below the velocity cut-off [73, 76].

Speckle tracking overcomes one of the major limitations of conventional Doppler techniques, the angle dependency. Full 2D velocity fields were visualized in this work, including the presence of short-lived, complex patterns, such as vortices. These patterns would have been impossible to capture by a user during a conventional examination using Doppler, since angle correction in those regions is impossible. Furthermore, due to the limited frame rate, these short-lived events would be easily missed.

VI. Conclusion

Overall, the straight tube validation measurements showed that both high frequency and conventional ultrasound ultrafast imaging were capable of providing reliable strain and flow information. The results obtained in the patient specific bifurcation phantom, - corroborated by the validation experiments - illustrated the ability to resolve complex strain and flow patterns throughout the cardiac cycle, without the prerequisite of contrast agents. Both strain and flow were derived from the same ultrasound acquisition allowing a seamless representation throughout the cardiac cycle. The use of high frequency as compared to conventional frequency ultrafast ultrasound is beneficial for accurately estimating high vessel wall strains and low velocity blood flow close to the vessel wall – lumen border. Due to the increased resolution, more local information can be obtained, however, the applicability is limited to 2 cm of depth. These above mentioned benefits might aid in establishing a more reliable characterization of atherosclerotic plaque geometry and progression. Finally, the choice of transducer center frequency should be based on the specific conditions concerning the vessel of interest, such as depth, anatomical features and the desired functional dynamics that need to be estimated.

Appendix

A. Phantom characterization

The Young's modulus estimation of both the validation vessel alone and within the surrounding was derived from the stress-strain relation (5) by measuring the strains induced in the phantom at various static pressure levels. Static pressure levels were obtained by connecting the vessel to a closed water circuit pressurized by a syringe and connected to a pressure sensor (TruWave pressure transducer, Edwards Lifesciences Corp. Irvine, CA). The applied pressures for the vessel alone ranged from 3.6 till 76.4 mmHg in 7 steps of ~ 10 mmHg. The pressure levels for the vessel within the surrounding ranged from 3.6 till 160.1 mmHg with increments of ~ 5 mmHg.

To measure strain, ultrasound plane wave acquisitions were performed for each intraluminal pressure level using the MS250 high frequency transducer in longitudinal position. The acquired channel data were beamformed using the delay and sum algorithm as described in the Methods section and averaged along the vessel axis. For strain estimation, automatic vessel wall delineation and diameter estimation were performed based on the RF data averaged along the vessel axis (see Fig. 9). Subsequently, the vessel wall edge crossings were found at predefined levels of the averaged RF signal.

When assuming no external pressure and a homogenous isotropic material, the mean circumferential strain ε_{θ_l}[77] for a thick walled tube at the lumen for a certain luminal pressure level *i* is given by,

$$\varepsilon_{\theta\_l}(i) = \frac{d_l(i) - \min d_l}{\min d_l} \tag{1}$$

Where d_l is the lumen diameter and mind_l is the diameter at a lower reference pressure. The mean circumferential σ_{θ_l} and radial σ_{r_l} stress [77] at the lumen, for a thick walled tube are given by,

$$\sigma_{\theta\_l}(i) = \frac{P_l(i) \cdot (d_l(i)/2)^2}{(d_v(i)/2)^2 - (d_l(i)/2)^2} \cdot \left(\frac{(d_v(i)/2)^2}{(d_l(i)/2)^2} + 1\right) \tag{2}$$

$$\sigma_{r\_l}(i) = \frac{P_l(i) \cdot (d_l(i)/2)^2}{(d_v(i)/2)^2 - (d_l(i)/2)^2} \cdot \left(-\frac{(d_v(i)/2)^2}{(d_l(i)/2)^2} + 1\right) \tag{3}$$

With P_l the intraluminal pressure and d_v the vessel diameter. Combined radial and circumferential stress σ_l, when assuming near incompressibility with a Poisson's ν ratio of 0.495 and zero longitudinal strain, is given by,

$$\sigma_l(i) = (1+\nu) \cdot \left((1-\nu) \cdot \sigma_{\theta\_l}(i) - \nu \cdot \sigma_{r\_l}(i)\right) \tag{4}$$

Assuming linear elastic material properties, the Young's modulus (E) can be estimated by linear fitting of the stress strain relations of both conditions, as depicted in Fig. 10. In case of pre-strain or pre-stress the Young's modulus is given by the first derivative of the stress strain relation,

$$E = \frac{d\sigma_l}{d\varepsilon_{\theta\_l}} \quad (5)$$

The Young's modulus of the validation vessel phantom was estimated by the stress strain relations depicted in Fig. 10. The lumen diameter range for the vessel was 4.82 mm to 6.54 mm and 4.80 mm to 5.81 mm with a wall thickness range of 1.43 mm to 1.23 mm and 1.43 mm to 1.37 mm for the validation vessel and the validation vessel with surrounding, respectively. Fig. 10 shows the linear LSQ fit yielding an E = 85 ± 2 kPa for the single vessel and an effective E = 225 ± 3 kPa for the validation vessel embedded in the surrounding body.

ACKNOWLEDGMENT

This work is part of the vernieuwingsimpuls VICI research programme with project number 12122 which is financed by the Netherlands Organisation for Scientific Research (NWO). The authors also want to gratefully acknowledge the technical support of Marleen van Aartrijk.

REFERENCES

[1] J. Klingelhofer, "Ultrasonography of carotid stenosis," *Cerebrovascular Diseases,* vol. 35, pp. 1-1, 2013.

[2] G. M. von Reutern, M. W. Goertler, N. M. Bornstein, M. Del Sette, D. H. Evans, A. Hetzel, *et al.*, "Grading Carotid Stenosis Using Ultrasonic Methods," *Stroke,* vol. 43, pp. 916-921, Mar 2012.

[3] E. G. Grant, C. B. Benson, G. L. Moneta, A. V. Alexandrov, J. D. Baker, E. I. Bluth, *et al.*, "Carotid artery stenosis: grayscale and Doppler ultrasound diagnosis--Society of Radiologists in Ultrasound consensus conference," *Ultrasound Q,* vol. 19, pp. 190-8, Dec 2003.

[4] R. S. Reneman, T. van Merode, P. Hick, and A. P. Hoeks, "Flow velocity patterns in and distensibility of the carotid artery bulb in subjects of various ages," *Circulation,* vol. 71, pp. 500-9, Mar 1985.

[5] M. M. Pedersen, M. J. Pihl, P. Haugaard, K. L. Hansen, T. Lange, L. Lonn, *et al.*, "Novel flow quantification of the carotid bulb and the common carotid artery with vector flow ultrasound," *Ultrasound Med Biol,* vol. 40, pp. 2700-6, Nov 2014.

[6] A. Harloff, F. Albrecht, J. Spreer, A. F. Stalder, J. Bock, A. Frydrychowicz, *et al.*, "3D blood flow characteristics in the carotid artery bifurcation assessed by flow-sensitive 4D MRI at 3T," *Magn Reson Med,* vol. 61, pp. 65-74, Jan 2009.

[7] K. L. Hansen, J. Udesen, F. Gran, J. A. Jensen, and M. Bachmann Nielsen, "In-vivo examples of flow patterns with the fast vector velocity ultrasound method," *Ultraschall Med,* vol. 30, pp. 471-7, Oct 2009.

[8] A. Swillens, P. Segers, and L. Lovstakken, "Two-dimensional flow imaging in the carotid bifurcation using a combined speckle tracking and phase-shift estimator: a study based on ultrasound simulations and in vivo analysis," *Ultrasound Med Biol,* vol. 36, pp. 1722-35, Oct 2010.

[9] B. Dunmire, K. W. Beach, K. Labs, M. Plett, and D. E. Strandness, Jr., "Cross-beam vector Doppler ultrasound for angle-independent velocity measurements," *Ultrasound in Medicine and Biology,* vol. 26, pp. 1213-35, Oct 2000.

[10] J. A. Jensen and P. Munk, "A new method for estimation of velocity vectors," *IEEE Transactions on Ultrasonics, Ferroelectrics, and Frequency Control,* vol. 45, pp. 837-51, 1998.

[11] G. E. Trahey, J. W. Allison, and O. T. von Ramm, "Angle independent blood flow detection by blood blow," *IEEE Transactions on Biomedical Engineering,* vol. 34, pp. 965-967, 1988.

[12] J. Kortbek and J. A. Jensen, "Estimation of velocity vector angles using the directional cross-correlation method," *IEEE Trans Ultrason Ferroelectr Freq Control,* vol. 53, pp. 2036-49, Nov 2006.

[13] A. V. Finn, M. Nakano, J. Narula, F. D. Kolodgie, and R. Virmani, "Concept of vulnerable/unstable plaque," *Arterioscler Thromb Vasc Biol,* vol. 30, pp. 1282-92, Jul 2010.

[14] E. Falk, "Pathogenesis of atherosclerosis," *J Am Coll Cardiol,* vol. 47, pp. C7-12, Apr 18 2006.

[15] J. A. Schaar, C. L. de Korte, F. Mastik, C. Strijder, G. Pasterkamp, P. W. Serruys, *et al.*, "Characterizing vulnerable plaque features by intravascular elastography," *Circulation,* vol. 108, pp. 2636-2641, 2003.

[16] J. Ophir, E. I. Céspedes, B. Garra, H. Ponnekanti, Y. Huang, and N. Maklad, "Elastography: ultrasonic imaging of tissue strain and elastic modulus in vivo," *European Journal Ultrasound,* vol. 3, pp. 49-70, 1996.

[17] J. Ophir, S. K. Alam, B. Garra, F. Kallel, E. Konofagou, T. Krouskop, *et al.*, "Elastography: ultrasonic estimation and imaging of the elastic properties of tissues," *Proc.Inst.Mech.Eng [H.],* vol. 213, pp. 203-233, 1999.

[18] C. L. de Korte, E. I. Céspedes, S. G. Carlier, A. F. W. van der Steen, G. Pasterkamp, D. Thompson, *et al.*, "Assessment of stiffness and elevated mechanical stress in atherosclerotic plaques by intravascular ultrasound: in vitro experience," *European Heart Journal,* vol. 19, p. 620, 1998.

[19] R. A. Baldewsing, J. A. Schaar, C. L. de Korte, F. Mastik, P. W. Serruys, and A. F. van der Steen, "Intravascular Ultrasound Elastography: A Clinician's Tool for Assessing Vulnerability and Material Composition of Plaques," *Stud.Health Technol.Inform.,* vol. 113, pp. 75-96, 2005.

[20] C. L. de Korte, "Strain estimation and/or hardness imaging of tissue or tissue structures," PCT Patent 60.708.879, 2005.

[21] C. L. de Korte, E. I. Céspedes, A. F. W. van der Steen, G. Pasterkamp, and N. Bom, "Intravascular ultrasound elastography: Assessment and imaging of elastic properties of diseased arteries and vulnerable plaque," *European Journal of Ultrasound,* vol. 7, pp. 219-224, 1998.

[22] C. L. de Korte, E. I. Céspedes, A. F. W. van der Steen, and C. T. Lancée, "Intravascular elasticity imaging using ultrasound: feasibility studies in phantoms," *Ultrasound Med.Biol.,* vol. 23, pp. 735-746, 1997.

[23] C. L. de Korte, M. M. Doyley, S. G. Carlier, F. Mastik, A. F. W. van der Steen, P. W. Serruys, *et al.*, "High resolution IVUS elastography in patients," Puerto Rico, USA, pp. 1767-1770.

[24] Y. Majdouline, J. Ohayon, Z. Keshavarz-Motamed, M. H. Roy Cardinal, D. Garcia, L. Allard, *et al.*, "Endovascular shear strain elastography for the detection and characterization of the severity of atherosclerotic plaques: in vitro validation and in vivo evaluation," *Ultrasound Med Biol,* vol. 40, pp. 890-903, May 2014.

[25] C. L. de Korte, G. Pasterkamp, A. F. W. van der Steen, H. A. Woutman, and N. Bom, "Characterization of plaque components using intravascular ultrasound elastography in human femoral and coronary arteries in vitro," *Circulation,* vol. 102, pp. 617-623, 2000.

[26] J. A. Schaar, E. Regar, F. Mastik, E. P. McFadden, F. Saia, C. Disco, *et al.*, "Incidence of high strain patterns in human coronary arteries: Assessment with three-dimensional intravascular palpography and correlation with clinical presentation," *Circulation,* vol. 109, pp. 2716-2719, 2004.

[27] H. H. Hansen, M. S. Richards, M. M. Doyley, and C. L. de Korte, "Noninvasive vascular displacement estimation for relative elastic modulus reconstruction in transversal imaging planes," *Sensors (Basel),* vol. 13, pp. 3341-57, 2013.

[28] H. H. G. Hansen, T. Idzenga, and C. L. de Korte, "Noninvasive Vascular Strain Imaging: from Methods to Application," *Current Medical Imaging Reviews,* vol. 8, pp. 37-45, Feb 2012.

[29] M. Cinthio, A. R. Ahlgren, T. Jansson, A. Eriksson, H. W. Persson, and K. Lindstrom, "Evaluation of an ultrasonic echo-tracking method for measurements of arterial wall movements in two dimensions," *IEEE Trans.Ultrason.Ferroelectr.Freq.Control,* vol. 52, pp. 1300-1311, 2005.

[30] H. Shi, C. C. Mitchell, M. McCormick, M. A. Kliewer, R. J. Dempsey, and T. Varghese, "Preliminary in vivo atherosclerotic carotid plaque characterization using the accumulated axial strain and relative lateral shift strain indices," *Phys.Med.Biol.,* vol. 53, pp. 6377-6394, 2008.

[31] M. Larsson, F. Kremer, P. Claus, T. Kuznetsova, L. A. Brodin, and J. D'Hooge, "Ultrasound-based radial and longitudinal strain estimation of the carotid artery: a feasibility study," *IEEE Trans Ultrason Ferroelectr Freq Control*, vol. 58, pp. 2244-51, Oct 2011.

[32] H. Hasegawa and H. Kanai, "Phase-Sensitive Lateral Motion Estimator for Measurement of Artery-Wall Displacement-Phantom Study," *Ieee Transactions on Ultrasonics Ferroelectrics and Frequency Control*, vol. 56, pp. 2450-2462, 2009.

[33] S. Korukonda, R. Nayak, N. Carson, G. Schifitto, V. Dogra, and M. M. Doyley, "Noninvasive vascular elastography using plane-wave and sparse-array imaging," *IEEE Trans Ultrason Ferroelectr Freq Control*, vol. 60, pp. 332-42, Feb 2013.

[34] H. H. Hansen, G. J. de Borst, M. L. Bots, F. L. Moll, G. Pasterkamp, and C. L. de Korte, "Compound Ultrasound Strain Imaging for Noninvasive Detection of (Fibro)Atheromatous Plaques: Histopathological Validation in Human Carotid Arteries," *JACC Cardiovasc Imaging*, vol. 9, pp. 1466-1467, Dec 2016.

[35] H. H. Hansen, G. J. de Borst, M. L. Bots, F. L. Moll, G. Pasterkamp, and C. L. de Korte, "Validation of Noninvasive In Vivo Compound Ultrasound Strain Imaging Using Histologic Plaque Vulnerability Features," *Stroke*, vol. 47, pp. 2770-2775, Nov 2016.

[36] C. Schmitt, G. Soulez, R. L. Maurice, M. F. Giroux, and G. Cloutier, "Noninvasive vascular elastography: Toward a complementary characterization tool of atherosclerosis in carotid arteries," *Ultrasound Med.Biol.*, vol. 33, pp. 1841-1858, 2007.

[37] R. L. Maurice, M. Daronat, J. Ohayon, E. Stoyanova, F. S. Foster, and G. Cloutier, "Non-invasive high-frequency vascular ultrasound elastography," *Physics in Medicine and biology*, vol. 50, pp. 1611-1628, 2005.

[38] F. Liu, Q. Yong, Q. Zhang, P. Liu, and Y. Yang, "Real-time tissue elastography for the detection of vulnerable carotid plaques in patients undergoing endarterectomy: a pilot study," *Ultrasound Med Biol*, vol. 41, pp. 705-12, Mar 2015.

[39] C. Naim, G. Cloutier, E. Mercure, F. Destrempes, Z. Qin, W. El-Abyad, *et al.*, "Characterisation of carotid plaques with ultrasound elastography: feasibility and correlation with high-resolution magnetic resonance imaging," *Eur Radiol*, vol. 23, pp. 2030-41, Jul 2013.

[40] H. Ribbers, R. G. Lopata, S. Holewijn, G. Pasterkamp, J. D. Blankensteijn, and C. L. de Korte, "Noninvasive two-dimensional strain imaging of arteries: validation in phantoms and preliminary experience in carotid arteries in vivo," *Ultrasound Med.Biol.*, vol. 33, pp. 530-540, 2007.

[41] C. Huang, X. Pan, Q. He, M. Huang, L. Huang, X. Zhao, *et al.*, "Ultrasound-Based Carotid Elastography for Detection of Vulnerable Atherosclerotic Plaques Validated by Magnetic Resonance Imaging," *Ultrasound Med Biol*, vol. 42, pp. 365-77, Feb 2016.

[42] M. Correia, J. Provost, M. Tanter, and M. Pernot, "4D ultrafast ultrasound flow imaging: in vivo quantification of arterial volumetric flow rate in a single heartbeat," *Phys Med Biol*, vol. 61, pp. L48-L61, Dec 7 2016.

[43] J. Bercoff, G. Montaldo, T. Loupas, D. Savery, F. Meziere, M. Fink, *et al.*, "Ultrafast compound Doppler imaging: providing full blood flow characterization," *IEEE Transactions on Ultrasonics, Ferroelectrics, and Frequency Control*, vol. 58, pp. 134-47, Jan 2011.

[44] S. Fadnes, I. K. Ekroll, S. A. Nyrnes, H. Torp, and L. Lovstakken, "Robust angle-independent blood velocity estimation based on dual-angle plane wave imaging," *IEEE Trans Ultrason Ferroelectr Freq Control*, vol. 62, pp. 1757-67, Oct 2015.

[45] I. K. Ekroll, T. Dahl, H. Torp, and L. Lovstakken, "Combined vector velocity and spectral Doppler imaging for improved imaging of complex blood flow in the carotid arteries," *Ultrasound Med Biol*, vol. 40, pp. 1629-40, Jul 2014.

[46] T. Mirault, M. Pernot, M. Frank, M. Couade, R. Niarra, M. Azizi, *et al.*, "Carotid stiffness change over the cardiac cycle by ultrafast ultrasound imaging in healthy volunteers and vascular Ehlers-Danlos syndrome," *J Hypertens*, vol. 33, pp. 1890-6; discussion 1896, Sep 2015.

[47] M. Tanter, J. Bercoff, L. Sandrin, and M. Fink, "Ultrafast compound imaging for 2-D motion vector estimation: application to transient elastography," *IEEE Trans.Ultrason.Ferroelectr.Freq.Control*, vol. 49, pp. 1363-1374, 2002.

[48] H. H. Hansen, A. E. Saris, N. R. Vaka, M. M. Nillesen, and C. L. de Korte, "Ultrafast vascular strain compounding using plane wave transmission," *J Biomech*, vol. 47, pp. 815-23, Mar 3 2014.

[49] S. Fekkes, A. E. Swillens, H. H. Hansen, A. E. Saris, M. M. Nillesen, F. Iannaccone, *et al.*, "2-D Versus 3-D Cross-Correlation-Based Radial and Circumferential Strain Estimation Using Multiplane 2-D Ultrafast Ultrasound in a 3-D Atherosclerotic Carotid Artery Model," *IEEE Trans Ultrason Ferroelectr Freq Control*, vol. 63, pp. 1543-1553, Oct 2016.

[50] I. K. Ekroll, A. Swillens, P. Segers, T. Dahl, H. Torp, and L. Lovstakken, "Simultaneous quantification of flow and tissue velocities based on multi-angle plane wave imaging," *IEEE Trans Ultrason Ferroelectr Freq Control*, vol. 60, pp. 727-38, Apr 2013.

[51] H. Hasegawa and H. Kanai, "Simultaneous imaging of artery-wall strain and blood flow by high frame rate acquisition of RF signals," *IEEE Trans.Ultrason.Ferroelectr.Freq.Control*, vol. 55, pp. 2626-2639, 2008.

[52] J. Luo and E. E. Konofagou, "Imaging of wall motion coupled with blood flow velocity in the heart and vessels in vivo: a feasibility study," *Ultrasound Med Biol*, vol. 37, pp. 980-95, Jun 2011.

[53] G. Montaldo, M. Tanter, J. Bercoff, N. Benech, and M. Fink, "Coherent plane-wave compounding for very high frame rate ultrasonography and transient elastography," *IEEE Transactions on Ultrasonics, Ferroelectrics, and Frequency Control*, vol. 56, pp. 489-506, Mar 2009.

[54] H. H. G. Hansen, R. G. P. Lopata, T. Idzenga, and C. L. de Korte, "An Angular Compounding Technique Using Displacement Projection for Noninvasive Ultrasound Strain Imaging of Vessel Cross-Sections," *Ultrasound in Medicine and Biology*, vol. 36, pp. 1947-1956, Nov 2010.

[55] H. H. G. Hansen, R. G. P. Lopata, T. Idzenga, and C. L. de Korte, "Full 2D displacement vector and strain tensor estimation for superficial tissue using beam-steered ultrasound imaging," *Phys Med Biol*, vol. 55, pp. 3201-3218, Jun 7 2010.

[56] A. E. Saris, H. H. Hansen, S. Fekkes, M. M. Nillesen, M. C. Rutten, and C. L. de Korte, "A Comparison Between Compounding Techniques Using Large Beam-Steered Plane Wave Imaging for Blood Vector Velocity Imaging in a Carotid Artery Model," *IEEE Trans Ultrason Ferroelectr Freq Control*, vol. 63, pp. 1758-1771, Nov 2016.

[57] A. E. Saris, M. M. Nillesen, S. Fekkes, H. H. Hansen, and C. L. de Korte, "Robust blood velocity estimation using point-spread-function-based beamforming and multi-step speckle tracking," in *IEEE Ultrasonics Symposium*, Taipei, Taiwan, 2015, pp. 1-4.

[58] R. F. Wagner, M. F. Insana, and S. W. Smith, "Fundamental correlation lengths of coherent speckle in medical ultrasonic images," *IEEE Trans Ultrason Ferroelectr Freq Control*, vol. 35, pp. 34-44, 1988.

[59] R. F. Wagner, S. W. Smith, J. M. Sandrik, and H. Lopez, "Statistics of Speckle in Ultrasound B-Scans," *IEEE Transactions on Sonics and Ultrasonics*, vol. 30, pp. 156-163, 1983.

[60] F. Kallel and J. Ophir, "A least-squares strain estimator for elastography," *Ultrason.Imaging*, vol. 19, pp. 195-208, 1997.

[61] R. Nayak, S. Huntzicker, J. Ohayon, N. Carson, V. Dogra, G. Schifitto, *et al.*, "Principal Strain Vascular Elastography: Simulation and Preliminary Clinical Evaluation," *Ultrasound Med Biol*, vol. 43, pp. 682-699, Mar 2017.

[62] F. Iannaccone, S. De Bock, M. De Beule, F. Vermassen, I. Van Herzeele, P. Verdonck, *et al.*, "Feasibility of a priori numerical assessment of plaque scaffolding after carotid artery stenting in clinical routine: proof of concept," *Int J Artif Organs*, vol. 37, pp. 928-39, Dec 2014.

[63] J. Fromageau, E. Brusseau, D. Vray, G. Gimenez, and P. Delachartre, "Characterization of PVA cryogel for intravascular ultrasound elasticity imaging," *IEEE Trans.Ultrason.Ferroelectr.Freq.Control*, vol. 50, pp. 1318-1324, 2003.

[64] B. Beulen, A. C. Verkaik, N. Bijnens, M. Rutten, and F. van de Vosse, "Perpendicular ultrasound velocity measurement by 2D cross correlation of RF data. Part B: volume flow estimation in curved vessels," *Experiments in Fluids*, vol. 49, pp. 1219-1229, Dec 2010.

[65] M. J. Pihl, M. B. Stuart, B. G. Tomov, M. F. Rasmussen, and J. A. Jensen, "A transverse oscillation approach for estimation of three-dimensional velocity vectors, part II: experimental validation,"

IEEE Trans Ultrason Ferroelectr Freq Control, vol. 61, pp. 1608-18, Oct 2014.

[66] S. Ricci, L. Bassi, and P. Tortoli, "Real-time vector velocity assessment through multigate Doppler and plane waves," *IEEE Trans Ultrason Ferroelectr Freq Control*, vol. 61, pp. 314-24, Feb 2014.

[67] B. W. A. M. M. Beulen, M. C. M. Rutten, and F. N. van de Vosse, "A time-periodic approach for fluid-structure interaction in distensible vessels," *Journal of Fluids and Structures*, vol. 25, pp. 954-966, Jul 2009.

[68] P. M. Morse and K. U. Ingard, "Theoretical Acoustics," in *Theoretical Acoustics*, ed: Princeton University Press, 1968, p. 949.

[69] H. C. Groen, F. J. Gijsen, A. van der Lugt, M. S. Ferguson, T. S. Hatsukami, A. F. van der Steen, *et al.*, "Plaque rupture in the carotid artery is localized at the high shear stress region: a case report," *Stroke*, vol. 38, pp. 2379-81, Aug 2007.

[70] H. C. Groen, F. J. Gijsen, A. van der Lugt, M. S. Ferguson, T. S. Hatsukami, C. Yuan, *et al.*, "High shear stress influences plaque vulnerability Part of the data presented in this paper were published in Stroke 2007;38:2379-81," *Neth Heart J*, vol. 16, pp. 280-3, Aug 2008.

[71] C. J. Slager, J. J. Wentzel, F. J. Gijsen, A. Thury, A. C. van der Wal, J. A. Schaar, *et al.*, "The role of shear stress in the destabilization of vulnerable plaques and related therapeutic implications," *Nat Clin Pract Cardiovasc Med*, vol. 2, pp. 456-64, Sep 2005.

[72] C. K. Zarins, D. P. Giddens, B. K. Bharadvaj, V. S. Sottiurai, R. F. Mabon, and S. Glagov, "Carotid bifurcation atherosclerosis. Quantitative correlation of plaque localization with flow velocity profiles and wall shear stress," *Circ Res*, vol. 53, pp. 502-14, Oct 1983.

[73] S. Fadnes, S. Bjaerum, H. Torp, and L. Lovstakken, "Clutter filtering influence on blood velocity estimation using speckle tracking," *IEEE Trans Ultrason Ferroelectr Freq Control*, vol. 62, pp. 2079-91, Dec 2015.

[74] C. Demene, T. Deffieux, M. Pernot, B. F. Osmanski, V. Biran, J. L. Gennisson, *et al.*, "Spatiotemporal Clutter Filtering of Ultrafast Ultrasound Data Highly Increases Doppler and fUltrasound Sensitivity," *IEEE Trans Med Imaging*, vol. 34, pp. 2271-85, Nov 2015.

[75] A. Yu and L. Lovstakken, "Eigen-based clutter filter design for ultrasound color flow imaging: a review," *IEEE Trans Ultrason Ferroelectr Freq Control*, vol. 57, pp. 1096-111, May 2010.

[76] C. A. Villagomez Hoyos, M. B. Stuart, K. L. Hansen, M. B. Nielsen, and J. A. Jensen, "Accurate Angle Estimator for High-Frame-Rate 2-D Vector Flow Imaging," *IEEE Trans Ultrason Ferroelectr Freq Control*, vol. 63, pp. 842-53, Jun 2016.

[77] S. P. Timoshenko and J. N. Goodier, *Theory of elasticity* vol. Third Edition. Singapore: McGraw-Hill, 1970.

Stein Fekkes studied Applied Physics at the Fontys academy in Eindhoven. He did his graduation project at the Radboud university medical center on myocardial lateral strain estimation using ultrasound. After receiving his bachelor's degree in 2004, he continued with the master Medical Engineering at the Eindhoven University of Technology (TU/e). In 2007 he did an internship at the Princess Margaret Hospital in Toronto, Canada where he developed an interstitial fluid pressure measurement analysis tool for cervix tumors. In 2009 he receives his master's degree with 4D dose accumulation using non-rigid deformation models, a graduation project performed at the Maastro Clinic in Maastricht. After almost 4.5 years of work in industry he decided to become PhD student as of November 2013 on ultrafast 3D carotid elastography.

Anne E.C.M. Saris studied Medical Engineering at the Eindhoven University of Technology (TU/e), The Netherlands. She did an internship at the Maastricht University Medical Center, The Netherlands, were she investigated dynamic contrast enhanced MRI of the aneurysm wall and quantification of microvasculature. In 2011-2012 she did her graduation project at the Radboud university medical center, Nijmegen, The Netherlands. She worked on correlation-based discrimination between myocardial tissue and blood in 3D echocardiographic images, for segmentation purposes. In April 2012, she received the degree of MSc in Medical Engineering. Since June 2012, Anne has been employed by the Medical UltraSound Imaging Center of the Radboud university medical center, Nijmegen, The Netherlands, where she is working as a PhD student on ultrafast blood velocity imaging.

Maartje M. Nillesen received her M.Sc. degree in mathematics (1999) from the University of Groningen, the Netherlands. After graduation she worked in the field of speech processing for several years, focusing on speech recognition by using a model of the human inner ear. In 2010 she obtained her Ph.D. degree from the Radboud University Medical Center where she worked on 3D automated segmentation in pediatric echocardiographic images. She is co-inventor of one patent and has authored or co-authored more than 20 peer-reviewed articles in national and international journals. She worked as a post-doctoral researcher at the Netherlands Heart Institute and the Medical UltraSound Imaging Center (MUSIC) of the Radboud University Medical Center respectively, where her research focuses on cardiac deformation assessment using ultrafast ultrasound imaging techniques. Her research interests include myocardial tissue characterization and 3D cardiac deformation imaging and 3D medical image segmentation, all using ultrasound imaging.

Jan Menssen received his Bachelor in in Electric Engineering in 1984. After graduating, he started his career at the Radboud University Medical Center in Nijmegen, the Netherlands as a research assistant at the Obstetrics department. Since then he has been employed at different departments at this medical center. Since 2005 he is a member of the Medical UltraSound Image Center (MUSIC). His research interests were fetal ECG, fetal pulse-oximetry, Surface EMG, NIRS and Ultrasound and he has co-authored more than 10 peer reviewed articles in these fields. At the MUSIC department his focus is on writing software.

Hendrik (Rik) Hansen obtained his M.Sc. degree in applied physics at the Eindhoven University of Technology, The Netherlands, in 2005. After graduating, Rik briefly worked as a software/system test engineer at Assembléon BV in Veldhoven, the Netherlands. Since 2007, Rik has been employed by the Medical UltraSound Imaging Center (MUSIC) of the Radboud University Medical Center, Nijmegen, the Netherlands. In 2012, he obtained his Ph.D. degree on noninvasive vascular ultrasound strain elastography for vulnerable plaque detection in carotid arteries. After obtaining his PhD degree, his research has mainly focused on developing ultrafast functional ultrasound techniques, such as 3D strain elastography, 3D blood flow imaging and shear wave elastography for vascular applications and breast cancer detection. Since November 2017 he has obtained a permanent position as leader of the functional ultrasound imaging workgroup of MUSIC. Rik has authored or co-authored over 30 peer-reviewed scientif articles in national and international journals and two book chapters.

Chris L. de Korte received his M.Sc. degree in electrical engineering from Eindhoven University of Technology, Eindhoven, The Netherlands, in 1993. He investigated the acoustical properties of eye tissues. In 1999, he obtained his Ph.D. degree in medical sciences at the Thoraxcenter, Erasmus University Rotterdam, The Netherlands on intravascular ultrasound elastography. In 2002, he joined the Clinical Physics Laboratory of the Radboud University Nijmegen Medical Center in Nijmegen, The Netherlands, as assistant professor and became head of it in 2004. In 2006, he was appointed as associate professor on medical ultrasound techniques and he finished his training as medical physicist in 2007. Since 2012, he has been head of the Medical UltraSound Imaging Center (MUSIC) of the Department of Radiology and Nuclear Medicine. He was appointed full professor on Medical Ultrasound Techniques in 2015. Since 2016 he is also full professor on Medical Ultrasound Imaging at the University of Twente, the Netherlands. He has authored or coauthored more than 140 peer-reviewed articles in international journals, inventor or co-inventor of four patents, and is recipient of the EUROSON Young Investigator award 1998 of the European Federation of Societies for Ultrasound in Medicine and Biology. His main research interests are functional imaging, acoustical tissue characterization, and photoacoustic imaging for (cardio-)vascular applications and for diagnosis, treatment monitoring, and guiding interventions in oncological applications.

TABLE I
TRANSDUCER PROPERTIES AND ACQUISITION PARAMETERS

Property	MS250	L12-5
Center frequency	21 MHz	8.9 MHz
Sampling frequency	62.5 MHz	35.7 MHz
Transducer element pitch	90 µm	195 µm
Nr. of transducer elements	256	256
Nr. of active transmit/receive elements	256	128
Transmit aperture size	23.04 mm	24.96 mm
Elevational focus width	1.0 mm[1]	1.6 mm[1]
Elevational focus depth	15 mm	18 mm
Axial resolution[2]	0.10 mm	0.16 mm
Lateral resolution[2]	0.15 mm	0.31 mm
Excitation signal	3-cycle pulse at center frequency	
Pulse repetition frequency	4 kHz	

[1]based on -6dB normalized pressure values
[2]based on simulated Verasonics acquisition of a point scatterer at elevational focus depth

TABLE II
BEAMFORMING PARAMETERS

	MS250	L12-5
Apodization window	Hamming	Hamming
F-number	0.875	0.875
Axial sampling beamforming grid	4.62 µm	10.8 µm
Lateral sampling beamforming grid	38.8 µm	48.5 µm

TABLE III
SETTINGS USED IN THE 2-STEP CROSS-CORRELATION-BASED DISPLACEMENT ESTIMATION ALGORITHM

			Vessel wall dynamics		Blood flow dynamics	
			L12-5	MS250	L12-5	MS250
Window size ± single sided search area [samples]	First iteration	Axial	33 ± 5	33 ± 11	129 ± 35	129 ± 81
		Lateral	5 ± 3	5 ± 3	31 ± 8	31 ± 10
	Second iteration	Axial	33 ± 4	33 ± 4	65 ± 10	65 ± 10
		Lateral	3 ± 3	3 ± 3	25 ± 10	25 ± 10
2D Median filtering [samples]	First iteration	Axial	-	-	7 x 13	7 x 13
		Lateral	-	-	7 x 13	7 x 13
	Second iteration	Axial	15 x 11[a]	15 x 11[a]	7 x 7	7 x 7
		lateral	31 x 23[a]	31 x 23[a]	7 x 7	7 x 7
2D interpolation of CC function			spline		cubic	
LSQSE window [samples]	Axial and axial shear		31 x 23	31 x 23	-	-
	Lateral and lateral shear		63 x 47	63 x 47	-	-

[a] Including edge detection

TABLE IV
CLUTTER FILTER CUT-OFF POINT FOR THE FIR FILTERS

	-3 dB	-10 dB	-20 dB	-40 dB	-70 dB
$v_{cut\text{-}off,axial}$ [cm/s]	1.18	0.7	0.39	0.16	0.025
$f_{cut\text{-}off}$ MS250[1]	0.159	0.096	0.053	0.021	0.003
$f_{cut\text{-}off}$ L12-5[1]	0.068	0.041	0.023	0.009	0.0015

[1]Normalized frequency, [$*f_{Nyquist}$]

This article has been accepted for publication in a future issue of this journal, but has not been fully edited. Content may change prior to final publication. Citation information: DOI 10.1109/TUFFC.2018.2834724, IEEE Transactions on Ultrasonics, Ferroelectrics, and Frequency Control

TABLE V
MEAN RELATIVE BIAS AND SD OF THE DISPLACEMENT AND STRAIN ESTIMATES OF THE MS250 AND L12-5 TRANSDUCERS

		MS250					L12-5			
		Displacement		Strain			Displacement		Strain	
		Mean Bias	Mean SD	Mean Bias	Mean SD		Mean Bias	Mean SD	Mean Bias	Mean SD
Superficial Surrounding	**A**	4.5%	2.2%	-20.5%	11.7 %	**E**	5.7%	1.9%	2.8%	11.9%
Superficial Wall	**B**	-3.5%	-2.5%	-61.8%	41.3 %	**F**	-9.6%	3.3%	-56.0%	10.7%
Deep Wall	**C**	-7.5%	-1.6%	-45.0%	11.7%	**G**	-11.3%	-2.5%	-58.3%	11.9%
Deep Surrounding	**D**	65.4%	-24.7%	27.9%	11.7 %	**H**	-5.8%	-7.4%	-5.5%	11.9%

TABLE VI
BIAS AND SD IN STRAIGHT VESSEL EXPERIMENTS

Beam-to-flow angle		90°		75°	
		MS250	L12-5	MS250	L12-5
|v|	Bias [%]	3.88	4.99	0.57	1.29
	SD [%]	1.20	3.41	1.69	4.05
Angle	Bias [°]	-0.04	0.07	-0.25	-0.10
	SD [°]	0.05	0.08	0.28	0.58

This article has been accepted for publication in a future issue of this journal, but has not been fully edited. Content may change prior to final publication. Citation information: DOI 10.1109/TUFFC.2018.2834724, IEEE Transactions on Ultrasonics, Ferroelectrics, and Frequency Control

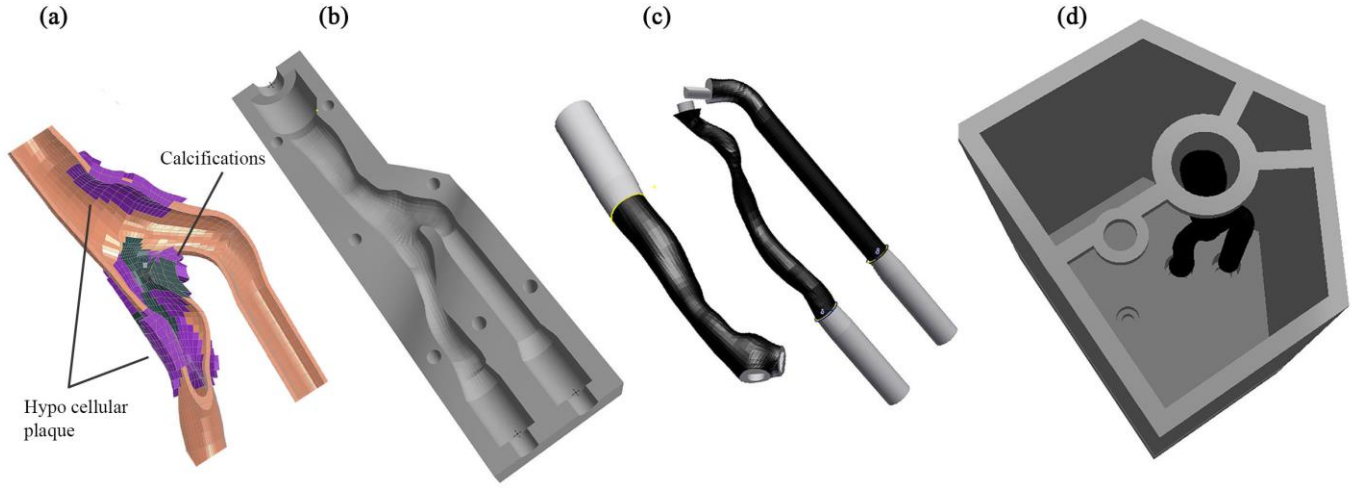

Fig. 1. (a) Longitudinal 3D view of the finite element model of an atherosclerotic carotid artery at the bifurcation based on a 75 year old male with an asymptomatic stenosis of 72% in the internal carotid artery. This figure shows only the intima (E = 250 kPa, v = 0.4999) in which different tissue types are modeled such as fatty plaques and calcifications which are distributed along the vessel wall. (b) Negative 3D single-sided mold definition of the FEM model of the vessel wall. (c) The lumen shape definition is detachable at the bifurcation enabling extraction after the PVA pouring process. (d) After the creation of the validation and CA vessel phantoms, they are positioned in the mold defining the surrounding tissue shape. Please note that the CA vessel is visualized in black while the validation vessel is absent in this schematic overview.

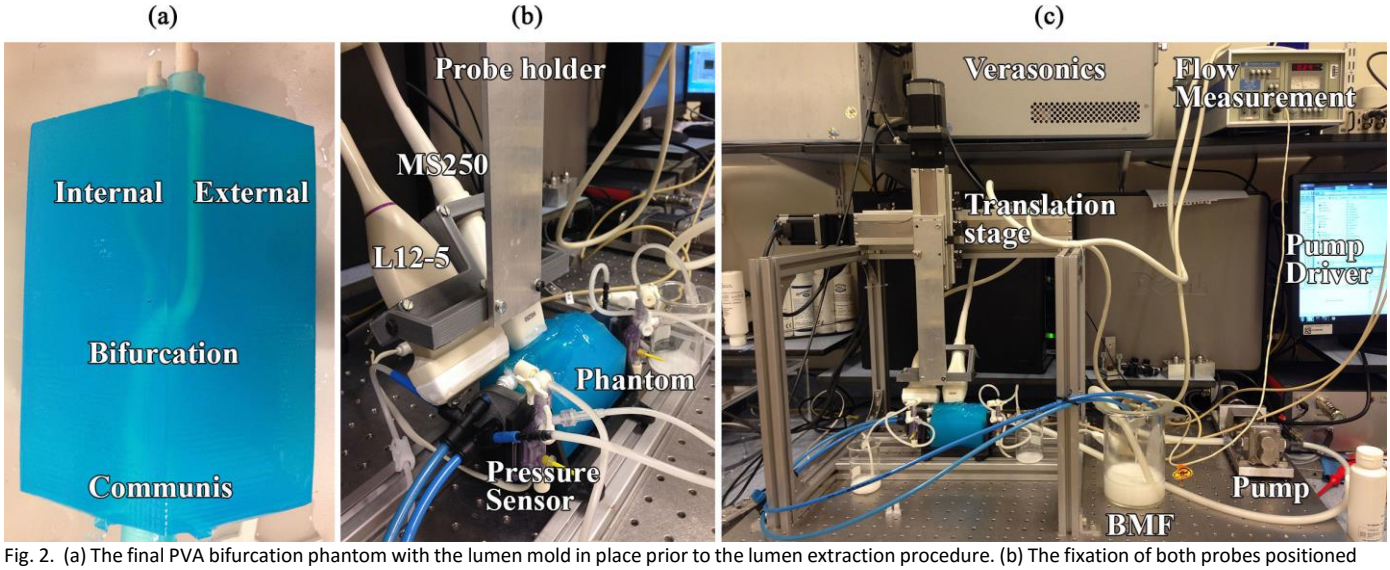

Fig. 2. (a) The final PVA bifurcation phantom with the lumen mold in place prior to the lumen extraction procedure. (b) The fixation of both probes positioned above the phantom attached to the translation stage. (c) An overview of the complete experimental setup where the blood mimicking fluid (BMF) is pumped through the phantom. The fluid enters the common carotid and exits through the internal and external vessels where the flow resistors were set such that equal outflow was guaranteed for both exit vessels. A custom made program (LabVIEW) enables pump control according to a realistic in vivo flow curve. The probes were connected to a Verasonics Vantage system acquiring plane wave ultrasound data at a PRF of 4 kHz.

This article has been accepted for publication in a future issue of this journal, but has not been fully edited. Content may change prior to final publication. Citation information: DOI 10.1109/TUFFC.2018.2834724, IEEE Transactions on Ultrasonics, Ferroelectrics, and Frequency Control

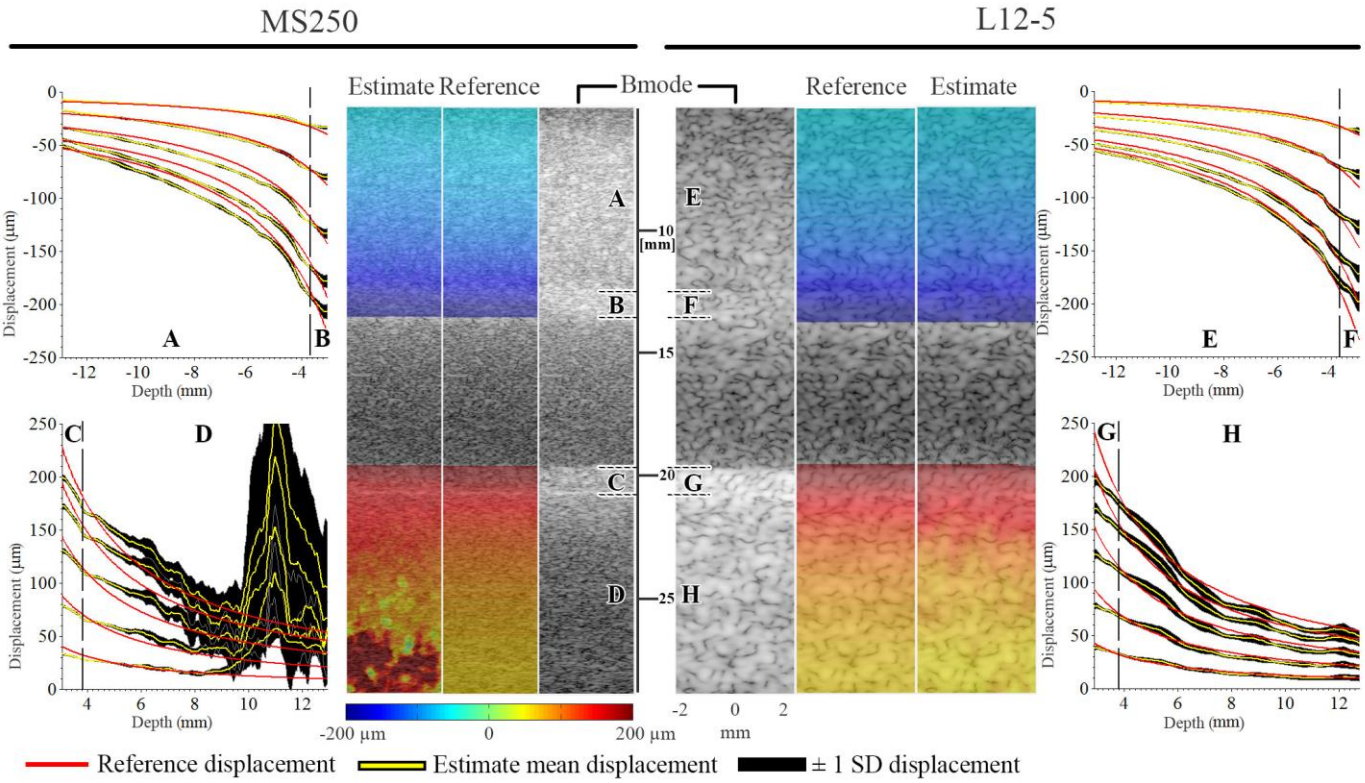

Fig. 3. B-mode representation overlaid with the color coded estimate and reference displacement of the straight validation vessel embedded in surrounding for both probes (center panel). Comparison of the estimated displacement profiles (yellow) and the reference displacement (red) divided into 4 spatial segments for the MS250 (A-D) and the L12-5 (E-H) (left and right panels). The dashed vertical line indicates the vessel wall surrounding transition.

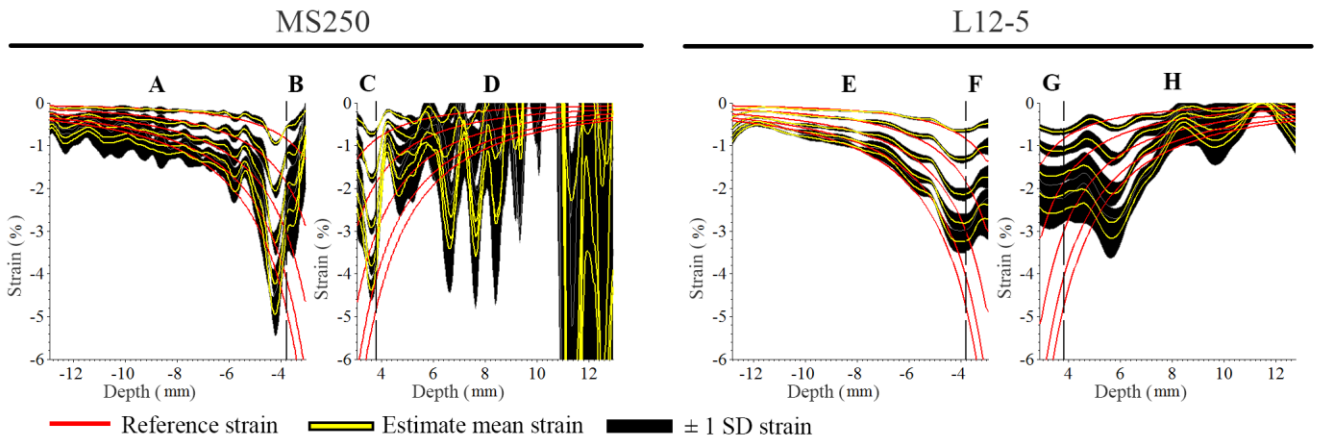

Fig. 4. Comparison between the estimates strain (yellow) and reference strain (red) profiles for both probes divided into 4 spatial segments for the MS250 (A-D) and the L12-5 (E-H). The dashed vertical line indicates the vessel wall surrounding transition.

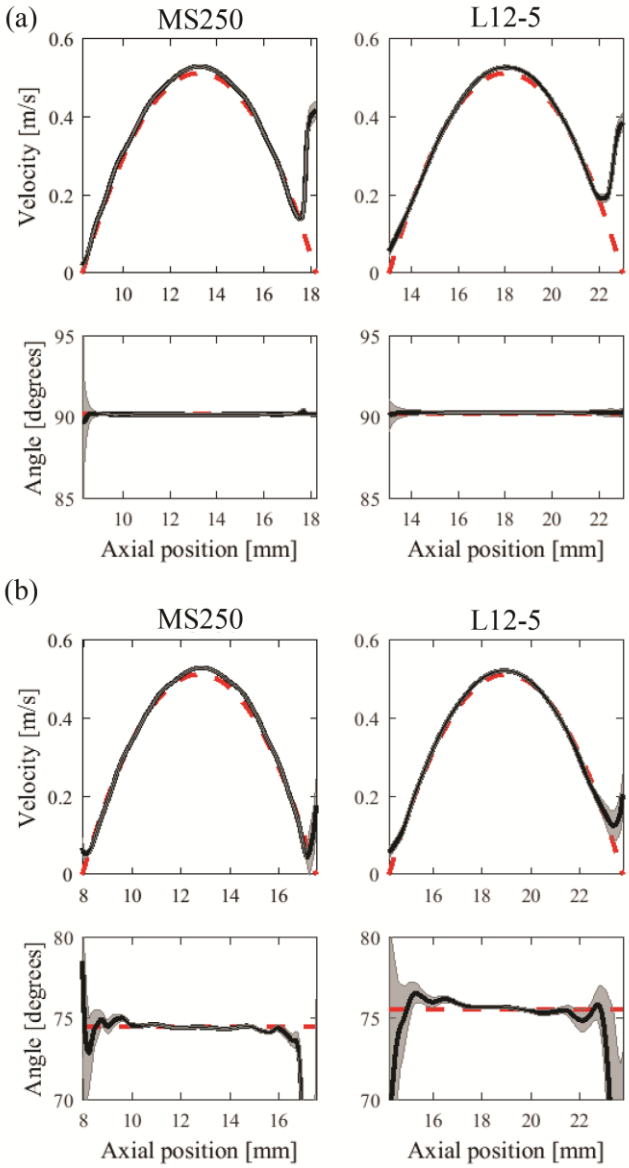

Fig. 5. Comparison between measured and true velocity profiles for the straight tube experiments. Panel (a) presents the results for a beam-to-flow angle of 90°, panel (b) for a beam-to-flow angle of 75°. The mean (black line) and standard deviation (±1 SD) of the measured velocity magnitude (top row) and velocity angle (bottom row) are compared to the theoretical profile (red dotted line).

This article has been accepted for publication in a future issue of this journal, but has not been fully edited. Content may change prior to final publication. Citation information: DOI 10.1109/TUFFC.2018.2834724, IEEE Transactions on Ultrasonics, Ferroelectrics, and Frequency Control

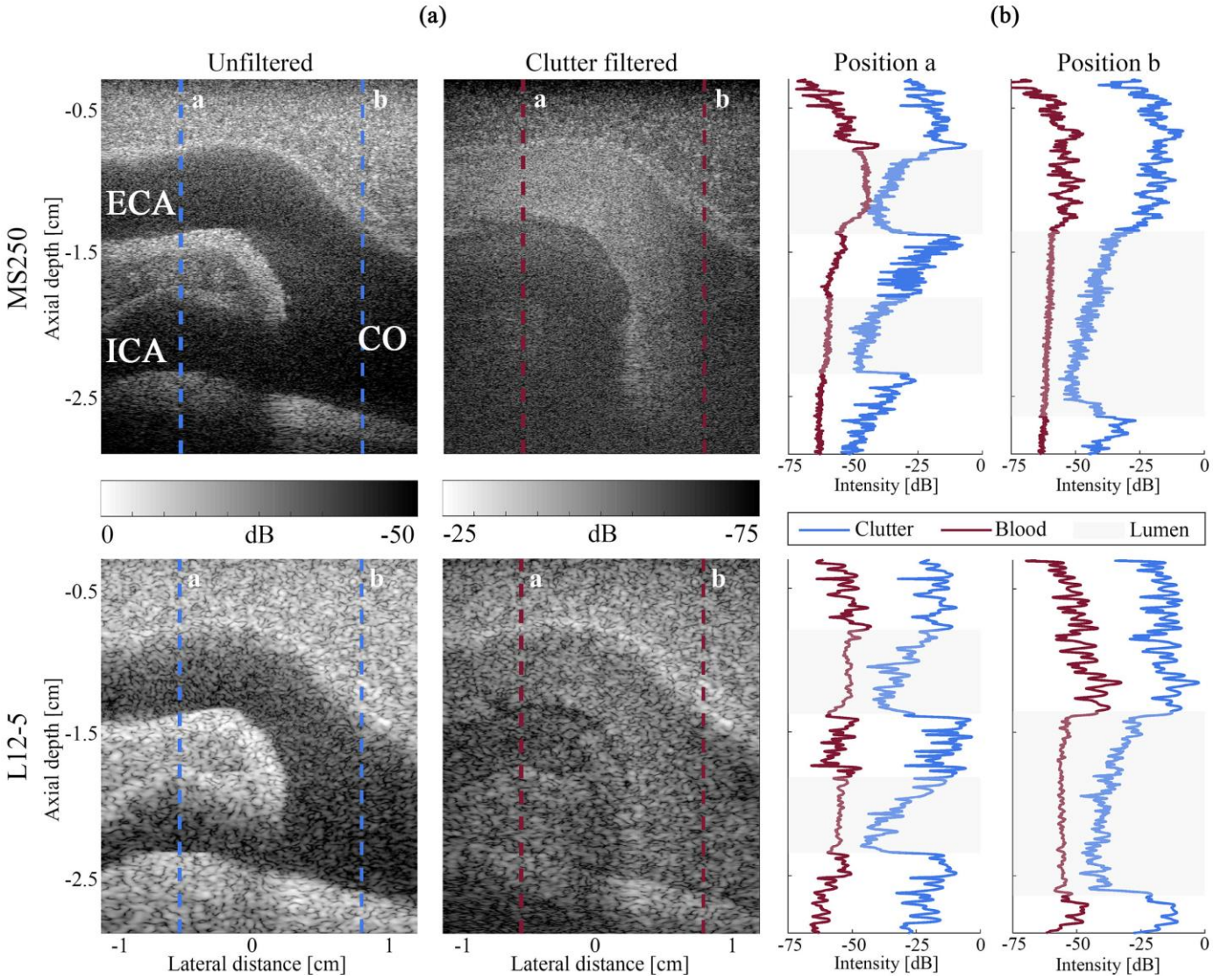

Fig. 6. (a) B-mode images of the bifurcation phantom with the Internal Carotid Artery (ICA), the External Carotid Artery (ECA) and the Communis (CO) before (left) and after (right) clutter filtering. (b) Mean blood and clutter signal intensities, averaged over one pressure cycle, for both the MS250 and L12-5 transducer, obtained at position a and b as indicated in the B-mode images. Gray panels correspond to the lumen areas.

This article has been accepted for publication in a future issue of this journal, but has not been fully edited. Content may change prior to final publication. Citation information: DOI 10.1109/TUFFC.2018.2834724, IEEE Transactions on Ultrasonics, Ferroelectrics, and Frequency Control

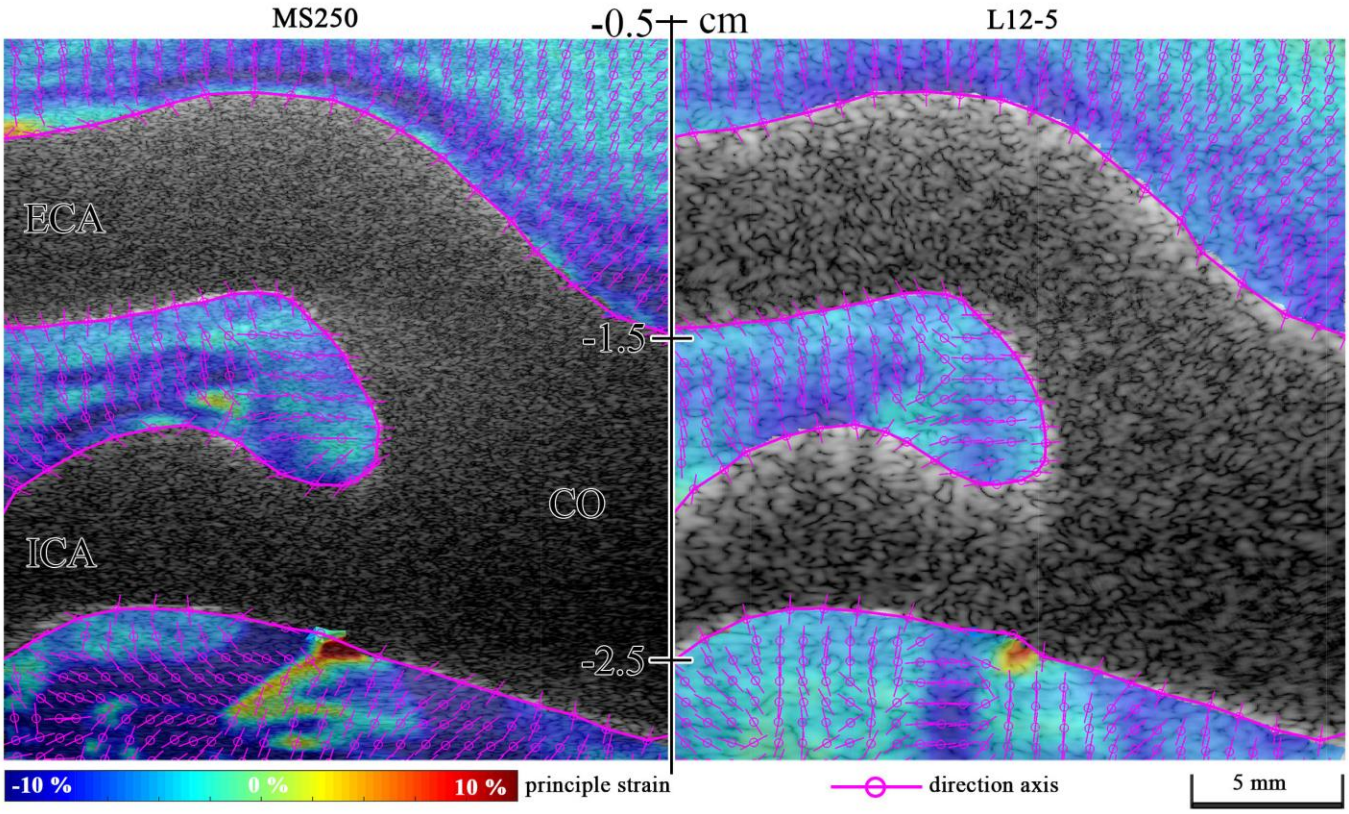

Fig. 7. B-mode representation overlaid with the principal strains for the high frequency probe MS250 versus the L12-5 probe at the minimum to maximum dilatation of the vessel present in the cardiac cycle. The principal strain overlay consist of a combination of strain components based on the maximum absolute value of eigenvalues and their corresponding eigenvector. This classification yields a strain map indicating the maximum deformation acting on the center of the specific eigenvector axis as depicted by the direction indicator. Please note that this could be either compressive or tensile deformations.

This article has been accepted for publication in a future issue of this journal, but has not been fully edited. Content may change prior to final publication. Citation information: DOI 10.1109/TUFFC.2018.2834724, IEEE Transactions on Ultrasonics, Ferroelectrics, and Frequency Control

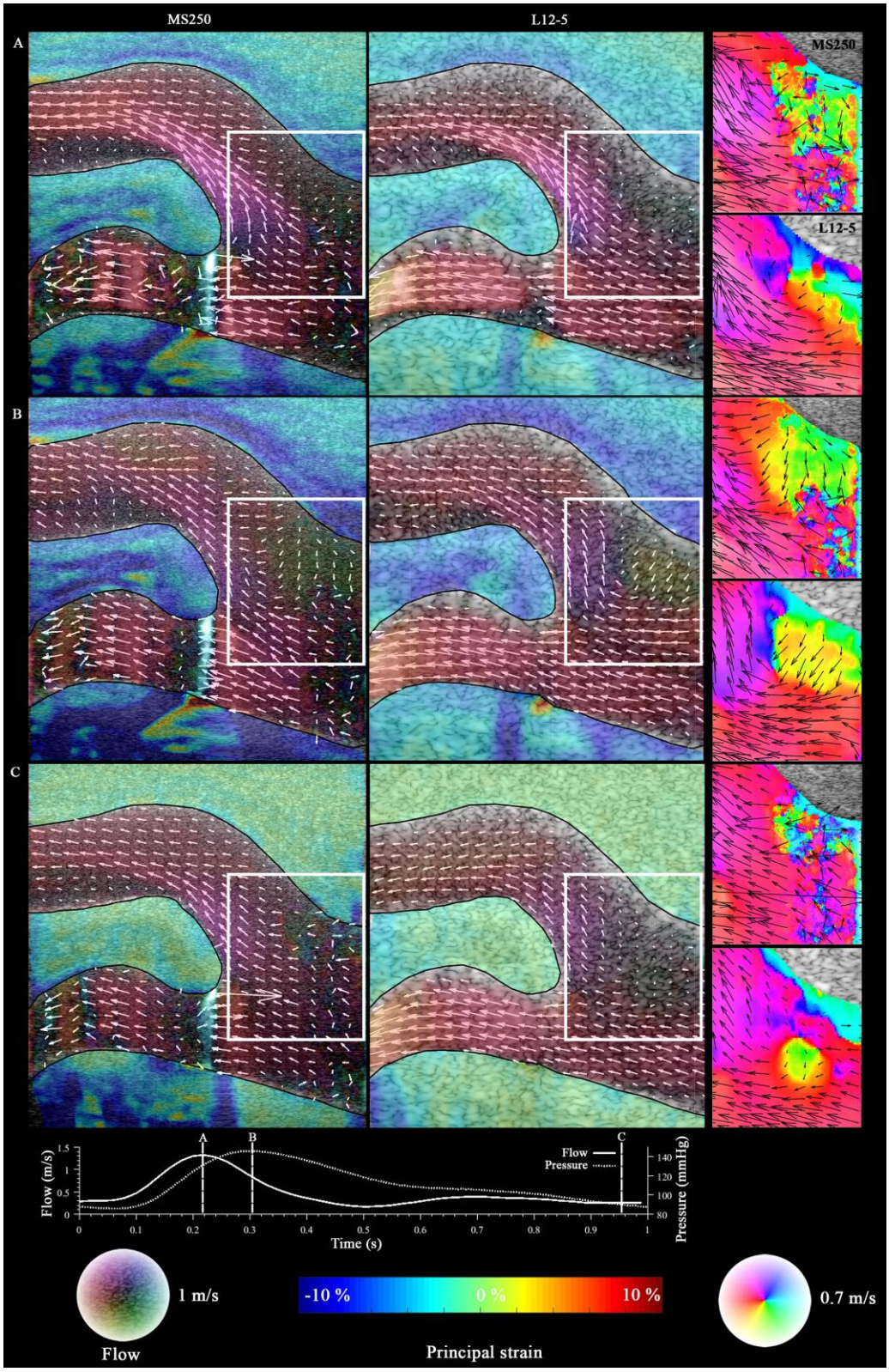

Fig. 8. B-mode images of the carotid bifurcation phantom overlaid with both the 2D blood velocity fields and the principal strains in the vessel wall and its surrounding, for three key time points during the cardiac cycle: (a) the peak systolic phase, where the highest blood velocities occur, (b) a frame in systolic deceleration, where peak strain values are observed, (c) A frame in late diastole, where low blood velocities and strain values are present. In the right column of the figure a zoomed region around the vortices is visualized. Please note the use of a different colorwheel, to emphasize the lower blood velocities present in this region. At the bottom of the figure, the flow and pressure curves are visualized for one cardiac cycle, with the time point A, B and C indicated. For a full overview of the results throughout the entire cardiac cycle, the reader is referred to the additional multimedia file: StrainAndBloodFlowDynamics.mp4. The movie shows the temporal evolution of the flow and strain patterns in the bifurcation phantom.

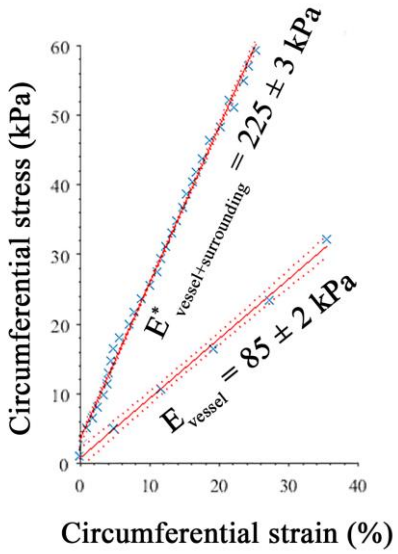

Fig. 9. A least squares linear fit of the stress strain relations in which the slope represents the Young modulus. E_{vessel} indicates the Young's modulus of the single validation vessel mounted at both ends and submerged in a water bad. $E^*_{vessel+surrounding}$ indicates the effective Young's modulus of the validation vessel embedded in the surrounding body. Please note the slight presence of pre-stress.

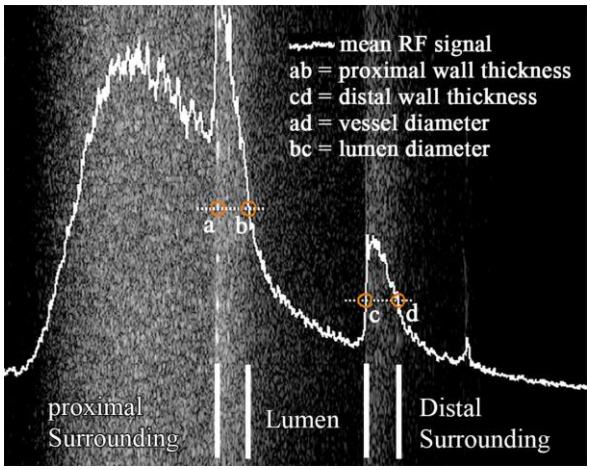

Fig. 10. B-mode representation of the validation vessel within the surrounding body overlaid with the RF signal averaged along the vessel axis. The vessel wall thickness and diameters are determined using the RF signal peak position and the crossing of the indicated levels b, c and d at multiple static pressure levels.